國立臺灣大學醫學院分子醫學研究所

碩士論文

Institute of Molecular Medicine

College of Medicine

National Taiwan University

Master's Thesis

磷酸化 Y14 與核酸之液態-液態相分離現象之研究

Characterization of liquid-liquid phase separation of phosphorylated Y14 and nucleic acids

洪珮瑜

Pei-Yu Hung

指導教授：譚婉玉 博士

Advisor: Woan-Yuh Tarn, Ph.D.

中華民國 114 年 7 月

July 2025

doi:10.6342/NTU202502570

國立臺灣大學碩士學位論文
口試委員會審定書
MASTER'S THESIS ACCEPTANCE CERTIFICATE
NATIONAL TAIWAN UNIVERSITY

論文中文題目：

磷酸化 Y14 與核酸液液相分離現象之性質描述

論文英文題目：

Characterization of liquid-liquid phase separation of phosphorylated Y14 and nucleic acids

本論文係 洪珮瑜 (學號：R12448012) 在國立臺灣大學 分子醫學研究所 完成之碩士學位論文，於民國 114 年 7 月 15 日承下列考試委員審查通過及口試及格，特此證明。

口試委員 Oral examination committee:

譚婉玉		
（指導教授 Advisor）		
孔倩伶	陳炜華	蔡欣祐

系（所、學位學程）主管 Director: 潘俊良

doi:10.6342/NTU202502570

誌謝

回顧這兩年碩士班時光，跌跌撞撞的時刻遠多於順利達成預期結果的片刻。過程中雖然感到痛苦，仔細回想卻也有不少成長，其中真的離不開許多人的幫忙與支持。首先，誠摯感謝我的指導教授譚婉玉老師，有耐心地給予我許多嘗試與探索的空間，在研究過程中傳授經驗、提供方向，您的專業讓我在這邊有了打開眼界的機會。另外也感謝陳瑞華老師、蔡欣祐老師以及林倩伶老師願意擔任我的論文指導與口試委員，感謝您們的用心與指導，提供許多寶貴的建議。此外，感謝學姊 Sabrina 在我初入實驗室時的協助，讓我更了研究內容。非常感謝助信宏學長，無私傳授蛋白純化技巧與 LLPS 相關實驗，給予實用的背景知識。感謝俊豪學長在 EMSA 實驗中一路的協助，並撥空幫我檢查、練習口試內容；感謝子瑋學姊在不同實驗中的幫助，也與學長一同協助學位口試的預備，讓我學到很多實驗以外的知識。也感謝久倫學長時常在實驗中給予建議。另外也感謝核心設施的周冠裕先生、秀容姊在顯微鏡及其他設備使用上的協助；感謝質譜中心，特別是鄭宇翔先生耐心指導我質譜的解讀。也感謝一路上幫助我實驗的人們。最後，我要深深感謝一路支持我的親朋好友，特別是我的家人們。在研究和課業都充滿挑戰、甚至生活型態經歷轉變的時刻，有你們做我最堅強的後盾，能永遠接住我脆弱的情緒、體諒我身心俱疲的狀態，無條件的接納與陪伴，讓我能夠一次次重新恢復力量，繼續努力向前。

doi:10.6342/NTU202502570

摘要

生物分子在時間與空間上的凝聚行為已被視為細胞於 DNA 雙股斷裂（DSBs）修復過程中的關鍵調控機制。多功能 RNA 結合蛋白 Y14/RBM8A 可於 DNA 損傷部位，透過與 RNA 介導的交互作用促進非同源性末端接合（NHEJ）的 DNA 修復途徑。Y14 具有帶電的內在無序區域（intrinsically disordered regions, IDRs），提供其進行液-液相分離（liquid-liquid phase separation, LLPS）的結構基礎。其 C 端 RS 重複序列經 SR 蛋白激酶 SRPK1 磷酸化後，可在鎂離子存在的條件下產生相分離現象。磷酸化後的 Y14（pY14）可形成動態凝聚物，並透過不同的交互作用方式與 DNA 損傷反應（DNA damage response, DDR）因子（如 Ku70/80）及核酸分子（包括長鏈非編碼 RNA 與 DNA）共同聚集。非磷酸化 Y14 與聚（ADP-核糖）（PAR）聚合物的結合親和力高於磷酸化的 Y14，表明 Y14 在被 SRPK1 磷酸化之前就被募集到 DNA 損傷處；隨後磷酸化的 Y14 在鎂離子存在下形成凝聚物。綜合本研究結果，Y14 經磷酸化後所引導的靜電驅動型相分離機制，與鎂離子協同調控，在 DNA 損傷位置上有助於修復因子的時空性募集與組織。

關鍵字：液態-液態相分離、磷酸化、二價陽離子、靜電作用、DNA 損傷修復

doi:10.6342/NTU202502570

Abstract

Spatiotemporal condensation of biomolecules has emerged as a critical mechanism for coordinating the DNA repair process at double-strand breaks (DSBs). The multifunctional RNA-binding protein Y14/RBM8A facilitates non-homologous end joining (NHEJ) through RNA-guided interactions at damage sites. Structurally, Y14 contains charged intrinsically disordered regions (IDRs) that provide the basis for its liquid-liquid phase separation (LLPS). SR protein kinase-1 (SRPK1)-mediated phosphorylation of C-terminal RS dipeptides enables Y14 to undergo magnesium-dependent LLPS *in vitro*. Phosphorylated Y14 (pY14) condensates accommodate DNA damage response (DDR) factors such as Ku70/80 and nucleic acids such as lncRNA *HOTAIRM1*. Non-phosphorylated Y14 bound poly(ADP-ribose) (PAR) polymers with a higher affinity than phosphorylated Y14, suggesting that Y14 is recruited to DNA lesions prior to its phosphorylation by SRPK1. Y14 forms condensates after phosphorylation with Mg^{2+} present. Together, our findings suggested electrostatic interaction-mediated LLPS for recruiting DNA repair factors to Y14 condensates at DNA damage sites.

Keywords: liquid-liquid phase separation, phosphorylation, divalent cation, electrostatic interaction, DNA damage repair

doi:10.6342/NTU202502570

Table of contents

doi:10.6342/NTU202502570

doi:10.6342/NTU202502570

doi:10.6342/NTU202502570

doi:10.6342/NTU202502570

Introduction

DNA repair is activated to maintain genome integrity

Deoxyribonucleic acid (DNA) encodes essential genetic information for replication, transcription, and inheritance; however, its integrity is constantly threatened by endogenous factors such as reactive oxygen species (ROS), replication stress, and hydrolysis, as well as exogenous insults including ultraviolet (UV) light, ionizing radiation, and chemotherapeutics [1, 2]. DNA lesions include single-strand breaks (SSBs), double-strand breaks (DSBs), base modifications, and inter-strand crosslinks. Among them, DSBs are the most lethal type due to their potential to induce genome instability or cell death [3]. To preserve genome stability, cells activate DNA damage response (DDR), which includes DNA repair [4], DNA damage tolerance pathways [5], cell cycle checkpoints [6, 7], transcriptional regulations [8], and others [9], with DNA damage repair playing a central role in maintaining genome integrity.

In mammals, DSBs are primarily repaired by homologous recombination (HR) and non-homologous end joining (NHEJ). HR relies on sister chromatids during late S/G2 phases, while NHEJ functions across the cell cycle by directly ligating DNA ends. The choice between these pathways depends on cell cycle phase, DNA end features, and

doi:10.6342/NTU202502570

chromatin structure [10]. Upon DSBs, poly(ADP-ribose) polymerase-1 (PARP-1) rapidly detects DNA ends and synthesizes poly(ADP-ribose) (PAR) chains to remodel chromatin and recruit repair proteins [11-13]. In canonical NHEJ, Ku70/80 heterodimers bind DNA ends and scaffold the recruitment of DNA-dependent protein kinase catalytic subunit (DNA-PKcs), which phosphorylates downstream substrates like Artemis, a 5' to 3' endonuclease, to process incompatible ends. DNA ligase IV (Lig4), with X-ray repair cross-complementing protein 4 (XRCC4) and XRCC4-like factor (XLF), then completes end ligation [14].

Beyond canonical enzymatic pathways, DNA repair research has expanded to encompass nuclear biophysics and transcriptional regulation. Notably, liquid-liquid phase separation (LLPS) has emerged as a mechanism by which repair proteins such as FUS, 53BP1, or MRNIP form membraneless condensates at damage sites, enhancing spatial organization and facilitating repair efficiency [15, 16]. DSBs also trigger the synthesis of damage-induced long non-coding RNAs (dilncRNAs), which act as scaffolds to recruit repair factors and, in some cases, promote their phase separation into dynamic compartments [17-19]. In addition, DDR rapidly activates RNA modifications, including N6-methyladenosine (m^6A), which is deposited at DNA breaks and is required for the

doi:10.6342/NTU202502570

recruitment of repair proteins such as polymerase κ [20, 21]. These RNA-guided and biophysical mechanisms offer emerging insights into how cells may organize repair processes in space and time, with LLPS increasingly recognized as a potential regulatory principle during DSB repair.

Liquid-liquid phase separation enables dynamic biochemical organization

Cells typically compartmentalize biochemical reactions using phospholipid bilayers, forming energy-consuming organelles [22]. In contrast, membrane-less organelles (MLOs) such as nucleoli, stress granules, and P bodies, achieve spatial organization through LLPS, a rapid and energy-efficient mechanism [23, 24]. Upon stimulation, macromolecules condense into liquid-like droplets that assemble biomolecules at specific loci, selectively enrich components, and package or isolate molecules to regulate diverse cellular processes [19, 25, 26].

To understand how LLPS enables dynamic compartmentalization, it is essential to explore its driving forces. Physically, increased biomolecular concentrations reduce system entropy, inducing phase separation into coexisting dense and dilute regions [27, 28]. Biochemically, scaffold proteins drive LLPS typically through two types of multivalent interactions. One involves conventional intermolecular contacts, such as

doi:10.6342/NTU202502570

protein-protein and protein-RNA interactions, while the other relies on weak, transient, multivalent forces between intrinsically disordered regions (IDRs) or low-complexity domains (LCDs) of proteins, including π-π stacking, electrostatic interactions, cation-π contacts, and hydrophobic effects [29]. These interactions guide the selective recruitment of client molecules into condensates, which display hallmark features such as fusion and fission, spherical shape, fluidity, and sensitivity to ionic strength, pH, or temperature [27, 28].

Regulatory mechanisms such as post-translational modifications (PTMs) and ionic microenvironments further fine-tune LLPS in DDR [30]. For example, PARylation by PARP1 initiates condensate formation, while PARG removes the PAR chains to dissolve them [31]. Phosphorylation of scaffold proteins, like Tau by MARK2, enhances LLPS but may drive irreversible aggregation under chronic stress [32]. Additionally, ionic microenvironments fine-tune condensate properties. Divalent cations such as Zn^{2+} act as structural regulators, facilitating TIA-1 phase separation through metal coordination that promotes multimerization and RNA binding, thus enabling incorporation into stress granules while preventing aberrant aggregation [33, 34].

doi:10.6342/NTU202502570

The role of liquid-liquid phase separation in DNA damage repair

Recent studies have revealed that LLPS contributes to various biological processes, including DNA damage repair [35], mRNA transcription [36-38], genome organization [39], immune response [40], and neuronal synaptic signaling [41]. During DDR, LLPS facilitates the rapid assembly of repair condensates at DSB sites, concentrating DNA repair factors to enhance repair efficiency [15, 42]. Unlike classical repair foci, these condensates exhibit liquid-like features such as fusion, dynamic protein exchange, and recapitulation *in vitro* that generally participate in every stage throughout DDR. Strikingly, approximately 10% of DDR-related proteins contain highly disordered regions (predictor of natural disordered regions (PONDR) score > 0.7), suggesting phase separation is a common regulatory feature in the repair machinery [43].

During the DSB sensing phase, LLPS drives the recruitment of PAR-associated proteins like FUS to damage sites, promoting Ku70/80 loading and γH2A.X cluster formation [31, 44]. In signal transduction, LLPS condensates facilitate MRN complex accumulation via MRNIP droplets and promote ATM activation [43], while SUMOylated RNF168 undergoes phase separation that limits its accessibility to DSB sites, thereby fine-tuning signal propagation [45]. As repair progresses, the formation of 53BP1

doi:10.6342/NTU202502570

condensates is essential for coordinating DSB resolution and cell cycle checkpoint control [46, 47]. Moreover, non-POU domain-containing octamer-binding (NONO) droplets help define repair pathway preference by recruiting DNA-PK and nuclear EGFR, driving NHEJ [48].

Various damage-associated signals dynamically regulate how DNA repair proteins undergo phase separation at chromatin. For instance, dilncRNA promotes the condensation of 53BP1 and forms DNA–RNA hybrids that enhance HR [19]. PARylation of FUS by PARP1 induces phase separation at DSB sites, creating compartments enriched in repair machinery [49]. Chromatin modifications such as phosphorylation, ubiquitination, and methylation are recognized by functional domains on 53BP1, thereby promoting its phase separation at DNA damage sites [50]. Aberrant PTMs in LLPS-prone proteins have also been associated with disease pathogenesis [51].

Nucleic acids modulate liquid-liquid phase separation behavior

In addition to PTMs, environmental cues, and molecular interactions, nucleic acids contribute significantly to the regulation of LLPS. Several MLOs rely on RNA–protein interactions to mediate cellular functions, including P bodies for RNA storage [52], Cajal bodies for RNA processing and assembly [53], and paraspeckles for transcriptional

doi:10.6342/NTU202502570

control via sequestration of regulatory RNAs and proteins [54]. Extending beyond RNA metabolism, LLPS also governs chromatin organization. Heterochromatin protein 1α (HP1α), a key factor in chromatin condensation, centromere integrity, and heterochromatin formation, undergoes LLPS through oligomerization [55-57]. HP1α selectively co-phase separates with nucleosomes and H3K9me3-marked DNA to form transcriptionally repressive compartments, which dynamically dissolve during mitosis [58, 59].

Nucleic acids influence LLPS behavior through multiple parameters, including their concentration, sequence, structure, and stoichiometric ratios with proteins. For instance, RNA enhances FUS condensate formation at moderate concentrations but disrupts it when exceeding a threshold [60]. Similar concentration-sensitive behaviors are observed in p53 upon DNA or RNA binding [61, 62]. Enhancer sequences containing transcription factor binding sites for MED1 and OCT4 can trigger droplet formation at a low concentration, while higher enhancer density promotes larger transcriptional condensates [63]. Notably, Neat1 lncRNA enhances FUS LLPS despite high total nuclear RNA levels, whereas other tRNA or RNA suppress it, highlighting the sequence-selective role of RNA in LLPS regulation [64].

doi:10.6342/NTU202502570

Most nucleic acids lack defined tertiary structures, giving them intrinsic flexibility similar to protein IDRs and allowing participation in LLPS via weak multivalent interactions. The higher flexibility of nucleic acids makes them easier to undergo LLPS. This flexibility is reflected in sequence-dependent physical properties; for example, poly(T)-ssDNA and AT-rich dsDNA are softer and more capable of supporting droplet formation under high-salt conditions than poly(A)-ssDNA or GC-rich dsDNA [65]. In contrast, structured RNAs such as G-quadruplexes (G4) promote LLPS through defined interactions with themselves or partner proteins, including Ded1p and FUS [51, 66, 67].

In certain cases, nucleic acids induce subcompartmentalization within condensates, forming either dense cores or hollow vesicle-like structures. For example, polyA-RNA and the deadenylase CNOT7 segregate into distinct phases within FMRP–ACPRIN1 condensates, a spatial arrangement that may enhance the efficiency of RNA deadenylation [68]. Additionally, hollow condensates can arise when RNA is added at an imbalanced ratio with proteins. RPM, a positively charged and arginine-rich protein, forms a dense shell and hollow vesicle interiors when mixed with a higher RNA molar ratio [69]. These structures remain liquid and respond to external stimuli, reflecting their dynamic nature [68, 69]. Furthermore, nucleic acids can be linked to pathological phase transitions; for

doi:10.6342/NTU202502570

instance, RNA prevents FUS droplets from solidifying [60], while G4-containing r(CGG)99 RNA accelerates FMRpolyG aggregation, a process that can be reversed by G4-binding molecules such as PpIX [70]. Different nucleic acids modulate condensate properties in a system-dependent and structure-specific manner.

Multifunctional RNA processing factor Y14 participates in DNA damage repair and undergoes liquid-liquid phase separation

Y14, encoded by the RBM8A gene, is a conserved RNA processing factor containing an RNA recognition motif (RRM). As a core component of the exon junction complex (EJC), Y14 facilitates mRNA surveillance via the nonsense-mediated decay (NMD) pathway and enhances translation efficiency [71]. Beyond its canonical roles, Y14 also modulates alternative splicing of apoptosis-related genes, producing isoforms with divergent effects on cell fate [72, 73]. *In vitro*, SRSF protein kinase 1 (SRPK1) phosphorylates Y14 at a conserved RS repeat in its C-terminal region, a motif essential for protein interaction and localization [74].

Functional analyses have revealed that Y14 is essential for cell fate determination. Its depletion induced cell death, G2/M cell-cycle arrest, and apoptosis accumulation [75]. Mouse genetic studies further demonstrate its necessary role in cortical development [76,

doi:10.6342/NTU202502570

77]. Knockdown of Y14 leads to aberrant splicing and dysregulation of key regulatory factors such as p53β and p21, both of which are crucial for maintaining genomic integrity [75]. In megakaryocytes, Y14 loss activates the p53-p21 axis, resulting in impaired differentiation and reduced platelet production under genotoxic stress [78].

Recent studies indicate that Y14 directly interacts with DDR factors and contributes to efficient NHEJ repair. In contrast, overexpression of a non-phosphorylatable mutant, Y14-SA, reduces the repair efficiency and prevents its accumulation at DSB sites, underscoring the importance of Y14 phosphorylation in DNA repair [79]. Our previous study also identified *HOTAIRM1* as a Y14-associated lncRNA that functions in NHEJ repair and acts as a scaffold bridging Y14 to the NHEJ complex [80]. Structurally, Y14 contains two charged-enriched modular IDRs at its N- and C-terminal domains, enabling its salt-sensitive phase separation. We previously demonstrated that Y14 undergoes LLPS, and *in vitro* co-condensates with *HOTAIRM1* through electrostatic interactions, particularly via its arginine-rich domain [81]. This RNA-dependent condensation provides a potential mechanism by which Y14 and *HOTAIRM1* contribute to the assembly of DNA repair-related condensates.

doi:10.6342/NTU202502570

Aims

Phosphorylation of Y14 is known to be essential for its accumulation at DSB sites and the promotion of efficient DNA damage repair. Although Y14 has been shown to undergo LLPS, it remains unclear whether the phosphorylated form also forms condensates or contributes to LLPS-mediated DNA repair. This study aims to characterize the LLPS behavior of phosphorylated Y14 and examine its interactions with nucleic acids.

doi:10.6342/NTU202502570

Results

SRPK1 phosphorylates Y14 in cells

Previous studies demonstrated that Y14 participates in DNA double-strand break (DSB) repair [79] [79, 80]. We previously reported that Y14 exists primarily in a phosphorylated form in cells, and that serine/arginine-rich splicing factor protein kinase-1 (SRPK1) phosphorylates its C-terminal RS dipeptides at Ser166 and Ser168 *in vitro* ([82], Fig. 1A). Moreover, deletion of the C-terminal region of Y14 (Y14-ΔC) or the non-phosphorylatable Y14 mutant (Y14-SA) impaired DSB repair efficiency [79, 81]. Our recent data further demonstrate that both Y14-ΔC and Y14-SA fail to localize to laser-induced DNA damage sites. The Ku heterodimer interacts more strongly with phosphorylated Y14 than with its non-phosphorylated form [79]. In addition, Y14 recruitment to DNA damage sites was abolished not only by SRPK1 inhibition but also upon treatment with PARP, ATM, ATR, or DNA-PK inhibitors. These findings suggest that Y14 phosphorylation is critical for its recruitment to DSB sites and efficient repair.

To investigate whether Y14 is a substrate of DNA damage response (DDR) kinases, we performed *in vitro* kinase assays and analyzed phosphorylation using Phos-tag SDS-

doi:10.6342/NTU202502570

PAGE, which retards the mobility of phosphorylated proteins. Both ATM and DNA-PK induced a clear mobility shift of recombinant Y14 (Appendix 1A, lanes 3 and 4), comparable to SRPK1-phosphorylated Y14 used as a positive control (Appendix 1A, lane 2), indicating that all three kinases phosphorylate Y14 *in vitro*. Mass spectrometry analysis identified an RSRS-containing phosphopeptide with one or two mass shifts of ~79.97 Da, consistent with mono- or di-phosphorylation. Fragment ion spectra confirmed phosphorylation at Ser166 and Ser168 (Appendix 1B). Although mass shifts were directly visualized only for SRPK1-phosphorylated Y14 (Appendix 1B), peptide-spectrum match (PSM) counts indicated robust modification at the same sites by DNA-PK and ATM as well (Appendix 1C), suggesting that all three kinases can target the C-terminal RSRS motif *in vitro*.

Although all tested kinases phosphorylated Y14 in the *in vitro* kinase assay, mass spectrometry revealed additional phosphorylation events outside the RS dipeptides, including modifications on tyrosine, serine, and threonine residues. These modifications likely resulted from using excess kinase and a single substrate *in vitro*. To assess whether SRPK1 or DDR kinases are responsible for Y14 phosphorylation *in vivo*, we treated U2OS cells with selective kinase inhibitors and analyzed endogenous Y14 by Phos-tag

doi:10.6342/NTU202502570

SDS-PAGE. Inhibition of SRPK1 using SRPIN340 caused a marked mobility shift indicative of Y14 dephosphorylation, comparable to that observed with alkaline phosphatase treatment (negative control) (Fig. 1B, lanes 1, 2, and 6). This dephosphorylation is consistent with our observation that Y14 fails to localize to DNA damage sites upon SRPIN340 treatment. In contrast, treatment with ATM (KU55933), DNA-PK (NU7441), or ATR (VE-821) inhibitors did not alter Y14 mobility on Phos-tag gels (Fig. 1B, lanes 3–5), despite these treatments abolishing Y14 recruitment to damage sites. Although inhibition of these DDR factors disrupted Y14 localization to DNA damage sites, treatment with these inhibitors did not lead to detectable Y14 dephosphorylation. These observations suggest that Y14 phosphorylation may be regulated by factors other than these DDR kinases.

Mg^{2+} promotes phospho-Y14 to undergo LLPS

Several DDR factors, including 53BP1 [35], FUS [80], MDC1 [83], and MRNIP [84], are known to accumulate at DSB sites in a spatiotemporally coordinated manner to form phase-separated condensates. Structural prediction of Y14 revealed a modular, electrostatically charged architecture, with intrinsically disordered regions (IDRs) at both the N- and C-termini [81], a feature commonly associated with LLPS potential.

doi:10.6342/NTU202502570

Consistent with this, our previous study showed that recombinant S- and His-tagged Y14 undergoes reversible LLPS in vitro, forming dynamic, liquid-like droplets correlating with its role in DSB repair [81]. Furthermore, Y14 localization at laser-induced DSB stripes was abolished following treatment with 1,6-hexanediol (1,6-HD), a hydrophobic alcohol widely used to disrupt weak intermolecular interactions within phase-separated condensates [85], suggesting that Y14 engages in LLPS at DSB sites.

To further understand how Y14 may function in DSB repair via LLPS, we re-evaluated the phase behavior of its phosphorylated form, as Y14 is predominantly phosphorylated in cells. We first expressed and purified non-tagged Y14 by generating a 6×His–GB1–TEV–Y14 fusion construct. The recombinant protein was purified using nickel NTA affinity chromatography, followed by fast protein liquid chromatography (FPLC) to eliminate potential nucleotide contaminants. TEV protease digestion was used to remove the fusion tag, yielding non-tagged Y14 (Appendix 2). *In vitro* phosphorylation of purified Y14 was then carried out using SRPK1, and phosphorylation was confirmed via Phos-tag gel electrophoresis (Fig. 2A).

We characterized the LLPS behavior of phosphor-Y14 (hereafter termed pY14) using microscopy, turbidity measurements, and sedimentation assays to assess phase

doi:10.6342/NTU202502570

separation, along with fluorescence recovery after photobleaching (FRAP) to evaluate droplet fluidity (Fig. 2B). Our previous results showed that while unmodified Y14 readily formed spherical droplets at pH (~7.2), pY14 failed to form droplets at any tested pH (Appendix 3A). Y14 contains duplicated RS dipeptides, a feature shared with SR proteins, which are splicing regulators characterized by varying numbers of RS motifs [86]. Given that phosphorylated RS domains in SR proteins can be precipitated by magnesium ions [87], we examined whether magnesium influences the phase separation of pY14.

Although pY14 formed only a few droplets in the presence of Mg^{2+} alone at pH7.2 (Appendix 3B), the addition of 3% polyethylene glycol (PEG), a crowding agent known to promote LLPS *in vitro* [88], substantially enhanced droplet formation. This enhancement was Mg^{2+}-concentration-dependent, as shown by microscopy (Fig. 2C) and turbidity assays (Fig. 2D). In contrast, treatment with EDTA abolished droplet formation, resulting in smaller droplets and reduced OD_{340} signals (Appendix 3C), highlighting Mg^{2+} as a key factor in pY14 LLPS.

To further characterize pY14 droplet formation, we performed a sedimentation assay (Fig. 2B and Methods). Since no visible pellet was observed after centrifugation, LLPS samples were analyzed by separating into top and bottom fractions. To validate the assay's

doi:10.6342/NTU202502570

ability to distinguish phase-separating behavior, we tested full-length Y14 (Y14-FL) and the previously reported non-phase-separating mutant Y14-ΔC [81] as positive and negative controls, respectively. SDS-PAGE analysis showed that Y14-FL was enriched in the lower fraction under droplet-forming conditions, whereas Y14-ΔC remained evenly distributed across both fractions (Fig. 2E), supporting the reliability of our approach. We then applied the same assay to pY14. In the presence of Mg^{2+} alone, pY14 exhibited minimal sedimentation (Appendix 3D), with signal detected in both upper and lower fractions, consistent with limited droplet formation observed by microscopy (Appendix 3B). In contrast, the addition of 3% PEG markedly enhanced pY14 sedimentation in a Mg^{2+}-dependent manner (Fig. 2F).

FRPA analysis confirmed that pY14 droplets formed in the presence of Mg^{2+} and PEG exhibit fluidity, similar to Y14 droplets (Fig. 2G). Notably, Y14 droplets formed under the same conditions showed reduced fluidity (Appendix 3E), as discussed in the following section. Together, these *in vitro* results demonstrate that Mg^{2+} facilitates LLPS of phosphorylated Y14. Supporting this notion in cells, we found that Y14 failed to localize at laser-induced DNA damage stripes upon EDTA treatment, which chelates intracellular Mg^{2+}. This suggests that Mg^{2+} is also required for Y14 condensate formation

doi:10.6342/NTU202502570

at DSB sites, possibly enabling its function in DNA repair.

NHEJ factors engage charged IDRs to partition into Y14-driven condensates

Phase-separating biomolecules often serve as scaffolds that promote condensate formation and selectively enrich client molecules [89]. Y14 has been reported to interact with Ku70/80 and is essential for their recruitment to DSB sites [79]. Our previous findings indicated that EDTA treatment significantly disrupts Ku70/80 accumulation at DSBs, suggesting that Ku heterodimers may participate in Y14-mediated LLPS. To test this hypothesis, we examined whether pY14 forms condensates that recruit Ku70/80 *in vitro*. Under Mg^{2+}/PEG conditions, Alexa Fluor 488–labeled Ku70/80 was observed to partition into pY14 droplets (Fig. 3A). In addition, our colleague found that this partitioning was abolished when Mg^{2+} was chelated by EDTA, which also disrupted pY14 droplet formation.

Building on our earlier observation that Y14 harbors charged IDRs and undergoes LLPS via electrostatic interactions [81], as well as Appendix 4A and B, we investigated potential client specificity. We analyzed the IDRs of DDR proteins using MobiDB (https://mobidb.org/) and evaluated charge properties via CIDER (https://pappulab.wustl.edu/CIDER/). A substantial number of DDR factors were found

doi:10.6342/NTU202502570

to contain charged IDRs (Appendix 4A), including NHEJ factors (such as Ku70/80, DNA-PK, Artemis, and XRCC4), DDR mediators (such as PARP and 53BP1), and DSB sensors (such as components of the MRN complex). Fraction of charged residues (FCR) analysis indicates most IDRs showed notable charge enrichment (Appendix 4A; f+, f-, and FCR), with several displaying modular charge distribution patterns (Appendix 4B). Both Ku70 and Ku80 possess two distinct charged IDRs. Considering their unique charge profiles, we asked whether the Ku heterodimer could co-phase separate into pY14 condensates via electrostatic interactions. Based on net charge per residue (NCPR) analysis [90], the Ku70-2 IDR exhibits a slightly positive net charge (NCPR = 0.037), distinguishing it from the other Ku70 and Ku80 IDRs, which are all negatively charged. To address this, we synthesized TAMRA-labeled peptides corresponding to Ku70 IDRs, one with a net weak positive charge and one with a net negative charge (Appendix 4C, top and middle). For comparison, we included a peptide from the DDR factor Artemis, which possesses an IDR with minimal net charge (Appendix 4C, top and middle).

Partitioning assays performed by our colleague revealed that only the negatively charged Ku70-2 peptide efficiently incorporated into pY14 droplets (Appendix 4C, bottom). Consistent with this, far-western blotting indicated that Ku70-2 bound more

doi:10.6342/NTU202502570

robustly to immobilized pY14 than the other IDR peptides (Fig. 3B and C). These observations reinforce our previous conclusion that the positive residues of Y14 contribute more substantially than its negative ones to driving LLPS [81]. This further supports our earlier proposition that the modular structure of Y14, characterized by alternating charges and a mildly negative net charge per residue (NCPR = -0.034), facilitates heterotypic LLPS with Ku70 via electrostatic interactions. Together, these data suggest that Y14 promotes the recruitment of NHEJ factors into repair condensates through charge-mediated interactions.

Nucleic acid partitioning into pY14 droplets

Previous studies have shown that Y14-associated lncRNA *HOTAIRM1* localizes at DNA damage sites and facilitates the recruitment of NHEJ factors by bridging Y14 and Ku70/80 [80]. Consistently, depletion of *HOTAIRM1* leads to delayed recruitment of Ku70/80 to DSB sites and attenuated DNA repair efficiency [80]. Recently, using an RNA-binding deficient mutant Y14-W73V, we found that Y14 failed to localize at DSB sites, suggesting that its recruitment is RNA-dependent. Moreover, knockdown of *HOTAIRM1* substantially impaired Y14 accumulation at DSB sites, indicating that Y14 localization is *HOTAIRM1*-dependent.

doi:10.6342/NTU202502570

We previously reported that RNA can co-phase separate with Y14 [81], but it remains unclear whether this also applies to phosphorylated Y14. To test this, we examined whether RNA molecules partition into pY14 droplets under Mg^{2+}/PEG conditions. Both full-length lncRNA *HOTAIRM1* (1,044 nt) and a synthetic short RNA (U25, 25 nt) readily partitioned into pY14 droplets (Fig. 4A), consistent with prior Y14 LLPS behavior [81]. Furthermore, Cy5-labeled *HOTAIRM1* co-partitioned with pY14 and Alexa Fluor 488-labeled Ku70/80 into the same droplets (Fig. 4B), forming composite ribonucleoprotein condensates. This observation is consistent with our previous findings that lncRNA *HOTAIRM1* facilitates the recruitment of NHEJ factors to DNA damage sites by acting as a molecular bridge between Y14 and DNA repair proteins [80].

To further explore how Y14 forms condensates at DSB sites, we synthesized a short Cy3-labeled double-stranded DNA (dsDNA, 70 bp) to mimic broken DNA ends. This dsDNA is partitioned into pY14 droplets (Fig. 4A), suggesting that pY14 directly interacts with DNA damage sites and potentially encapsulates broken DNA ends.

Interestingly, both dsDNA and lncRNA *HOTAIRM1* formed ring-like fluorescent structures along the periphery of pY14 droplets (Fig. 4A, enlarged frames), with the ring

doi:10.6342/NTU202502570

of *HOTAIRM1* appearing less pronounced than that of dsDNA. This prompted time-resolved confocal imaging to investigate the incorporation dynamics of nucleic acids into condensates. Over time, U25 rapidly and uniformly diffused into the droplet interior, while both *HOTAIRM1* and dsDNA initially accumulated at the periphery before gradually penetrating inward (Fig. 4C). Notably, *HOTAIRM1* exhibited a more persistent peripheral localization compared to dsDNA.

Upon co-incubation with dsDNA, the short RNA U25 readily entered the pY14 droplets, whereas *HOTAIRM1* predominantly remained at the droplet periphery, forming a distinct ring-like pattern (Fig. 4D). We speculated that molecular charge density and structural complexity dictate spatial partitioning within pY14 condensates, with smaller and less negatively charged RNAs accessing the droplet interior more rapidly than larger or highly charged species.

Y14 does not distinguish RNA m^{6}A modifications

Recent studies have revealed the importance of m^{6}A modification in regulating DNA repair and maintaining genome integrity during the DNA damage response [20, 91] (X1). Using photo-crosslinking-assisted m^{6}A-sequencing (PA-m^{6}A-seq), we previously identified an m^{6}A modification site at A827 in *HOTAIRM1* that conforms to the RRACH

doi:10.6342/NTU202502570

consensus motif [92] and is induced upon DNA damage. m^{6}A-RIP experiments further validated that HOTAIRM1 undergoes m^{6}A modification following DSB induction. Moreover, knockdown of the m^{6}A writer METTL3 significantly reduced Y14 accumulation at DSB sites, suggesting that m^{6}A-modified RNAs are involved in DSB repair. As both m^{6}A readers/writers and m^{6}A-modified RNAs have been implicated in promoting liquid–liquid phase separation (LLPS) [84, 93, 94], we investigated whether m^{6}A-modified *HOTAIRM1* could affect Y14 binding.

To address this, we *in vitro* transcribed the third fragment of *HOTAIRM1*, which has previously been shown to have strong Y14 binding affinity, with varying m^{6}A levels and radiolabeled it using [α-^{32}P] UTP (Appendix 5A and B). Electrophoretic mobility shift assay (EMSA) analysis revealed that m^{6}A modification did not significantly enhance Y14–RNA binding (Appendix 5C), although a slight increase in binding affinity was observed based on Kd values (Appendix 5D).

To further confirm the interaction between m^{6}A-modified RNA and Y14, we *in vitro* transcribed short RNA oligonucleotides containing varying numbers of m^{6}A modifications and labeled them at the 5' end using [γ-^{32}P] ATP (Appendix 6A-C). Unlike the longer 270-nt *HOTAIRM1* fragment used previously, these synthetic RNAs minimized

doi:10.6342/NTU202502570

potential confounding factors such as RNA secondary structure and length, allowing us to isolate the contribution of m^6A number. EMSA analysis and quantitative binding results showed that m^6A modification did not enhance the binding affinity between RNA and Y14 (Appendix 6D and E). This is likely due to the absence of a YTH domain in Y14 [95], which is commonly required for specific m^6A recognition. Therefore, the interaction between Y14 and *HOTAIRM1* is likely mediated solely by its RNA recognition motif (RRM), and the role of m^6A in DSB repair may not involve direct modulation of Y14 and RNA affinity. Instead, m^6A-modified *HOTAIRM1* may contribute to the DNA damage response through alternative mechanisms, such as facilitating Y14-associated phase separation or recruiting other m^6A reader proteins, possibilities that remain to be clarified.

Y14 interacts with PAR

As a primary DNA damage sensor, PARP1 rapidly detects DNA strand breaks and becomes activated through local structural rearrangements, catalyzing the synthesis of poly(ADP-ribose) (PAR) chains at damage sites. These PAR polymers serve as dynamic scaffolds that recruit RNA-binding proteins and DNA repair factors, facilitating the formation of repair condensates and orchestrating chromatin remodeling [96-100].

Depletion of Y14 or chelation of divalent cations by EDTA-AM reduced the

doi:10.6342/NTU202502570

accumulation of core NHEJ factors, such as Ku70, DNA-PK, LIG4, and XLF, at laser-induced DSB sites, while without altering PAR polymer localization. Furthermore, pharmacological inhibition of PARP1 with Olaparib abolished Y14 recruitment, indicating that PAR synthesis precedes Y14 localization to DSBs.

Because phosphorylation at the C-terminal arginine/serine (RS) dipeptide of Y14 is essential for its downstream functions in condensate formation and DSB repair, we next investigated whether its initial recruitment via PAR is contingent upon this modification. To address this, we performed an *in vitro* PAR-binding assay comparing unphosphorylated and phosphorylated forms of recombinant Y14. Using biotin-labeled PAR as bait, we performed pull-down assays with recombinant Y14 proteins and found that Y14, but not phosphorylated Y14, interacts more with biotin-PAR (Fig. 5A). Y14 -ΔC completely abolishes its affinity with PAR (Fig. 5A), consistent with the loss of DNA damage localization observed for both Y14-ΔC and the phosphorylation-deficient mutant Y14-SA. Notably, the C-terminal region of Y14 harbors an arginine/serine (RS) dipeptide repeat, previously identified as a phosphorylation target [82], suggesting its dual role in PAR interaction and post-translational regulation.

doi:10.6342/NTU202502570

Discussion

Biomolecular condensates formed via LLPS are increasingly recognized as functional organizers in DNA repair. In this study, we explored the role of Mg^{2+} in promoting phosphorylated Y14 to undergo LLPS, and tried to characterize its co-phase separation with nucleic acids.

The effects of DDR kinases on Y14 phosphorylation are indirect.

Phosphorylation of the C-terminal RS dipeptides is essential for Y14 localization at DSB sites, as shown by Y14-SA and Y14-ΔC. Given that Y14 remains predominantly phosphorylated regardless of DNA damage [81], it is likely phosphorylated constitutively by SRPK1. Although inhibition of ATM, ATR, or DNA-PK abrogates Y14 accumulation at damage sites, our colleague found that it does not affect Y14 phosphorylation or the localization of SRPK1, which remains present in both the nucleus and cytoplasm. While most phosphorylation events in DNA repair pathways are governed by DDR kinases [101-103], our findings suggest that DDR signaling influences Y14 recruitment through indirect or downstream mechanisms, rather than by regulating its phosphorylation status directly.

doi:10.6342/NTU202502570

pY14 droplets exhibit greater stability than Y14 under Mg^{2+}/PEG conditions.

Treatment with EDTA disrupted pY14 droplet formation and abolished the localization of Y14 and other core NHEJ factors at DSB sites. FRAP analysis revealed that pY14 droplets formed under Mg^{2+}/PEG conditions were less perturbed than Y14 droplets formed in the absence of Mg^{2+}/PEG, despite displaying comparable fluidity. Notably, Y14 droplets under the same Mg^{2+}/PEG conditions condensed into very small structures with extremely low mobility. These findings suggest that the cellular environment may preferentially support phosphorylated Y14 condensate formation.

Previous studies have demonstrated that chromatin rearrangement during mitosis can trigger ATP hydrolysis and lead to a transient rise in free Mg^{2+} levels [104]. Maeshima, K., et al. reported intracellular free Mg^{2+} concentrations of approximately 1 mM; combined with the additional release of Mg^{2+} (~1 mM) during ATP consumption in mitosis, this ionic environment is enough for condensation of highly negatively charged chromatin. Although the dynamics of Mg^{2+} in the context of DNA damage remain unexplored, Mg^{2+} may play a comparable role in promoting pY14-driven phase separation during DNA damage. This raises the possibility that chromatin remodeling during DNA damage could likewise be influenced by transient Mg^{2+} fluctuations,

doi:10.6342/NTU202502570

warranting further investigation. Interestingly, divalent cations have been reported to stabilize protein condensates [33, 105]. For example, Zn^{2+} promotes TIA-1 multimerization and phase separation for recruitment to stress granules in response to cellular stress [34]. Zn^{2+} also strongly induces tau protein LLPS, forming dynamic droplets even at low protein concentrations [106]. Together, these suggest that divalent cations, including Mg^{2+} and Zn^{2+}, broadly contribute to condensate regulation across distinct cellular contexts. In our study, Mg^{2+} plays a key role in facilitating LLPS of phosphorylated Y14 during DNA repair; however, whether other divalent cations contribute to pY14 condensate formation remains to be investigated.

pY14 co-phase separates with RNA and NHEJ factors via electrostatic interactions.

As shown in Fig. 3 and 4, RNAs and NHEJ factors co-condense with pY14 primarily through electrostatic complementarity. In Fig. 4C, lncRNA *HOTAIRM1* and short dsDNA initially accumulated at the droplet periphery before gradually diffusing into the interior, whereas the short RNA U25 promptly and uniformly entered the condensates. (Fig. 4C). These patterns likely reflect how RNA length, net charge, and structural complexity influence their partitioning into mildly negatively charged pY14 droplets (NCPR = −0.034). Less negatively charged molecules like U25 may diffuse into the droplet more

doi:10.6342/NTU202502570

readily, while highly charged or structured nucleic acids, such as *HOTAIRM1* and dsDNA, may be transiently excluded from the interior.

Co-incubation experiments revealed distinct spatial arrangements (Fig. 4D). With *HOTAIRM1* and dsDNA, *HOTAIRM1* remained peripheral while dsDNA entered the droplet core, forming a layered structure. In contrast, when dsDNA was added with U25, the dsDNA stayed outside while U25 diffused inward (Fig. 4D). These contrasting dynamics may be because the RNA molecular features, particularly charge and size, can influence the spatial organization of nucleic acids within condensates [107].

Additionally, previous data demonstrated that *HOTAIRM1* is not transcriptionally upregulated following DNA damage, but instead translocates into the nucleus upon DSBs [80]. Knockdown of *HOTAIRM1* not only delayed Ku70/80 accumulation at DSB sites but also compromised the efficiency of NHEJ repair [80]. While the peripheral localization of *HOTAIRM1* within pY14 condensates cannot be definitively linked to a functional role, its spatial positioning suggests a potential for interface-specific interactions, such as facilitating the recruitment of repair factors. Similar peripheral accumulation has been observed in other phase-separated systems, including lncRNA *NEAT1* in paraspeckles [108] and RNA-binding proteins at nucleolar boundaries [109],

doi:10.6342/NTU202502570

where interface positioning supports spatial compartmentalization. These parallels suggest that *HOTAIRM1* may act as a molecular guide at condensate interfaces, contributing to the localized coordination of DNA repair proteins. Further studies are needed to validate this potential role and clarify its mechanistic involvement.

Limitations of the study

For the sedimentation assay following traditional methods [110-114], although droplets were microscopically observed, no visible pellet was formed after centrifugation. Despite similar protein concentrations (20 μM) and droplet sizes (~3–5 μm), as reported in some of these references, sedimentation was not detected, indicating that factors beyond size or concentration may impede pellet formation. As an alternative, we adopted a fractionation strategy based on earlier reports [82, 115], in which LLPS samples were separated into upper and lower phases. While this approach diverges from conventional sedimentation protocols, it effectively separates condensate-enriched fractions.

doi:10.6342/NTU202502570

Materials and methods

Cell culture and drug treatment

U2OS cells were cultured in McCoy's 5A medium (Thermo Fisher Scientific) supplemented with 10% fetal bovine serum (FBS), 1% L-glutamine, and 50 μg/mL penicillin-streptomycin, and maintained at 37 °C with 5% CO_2. For inhibitor treatment, cells were treated with 10 μM KU55933 (ATM inhibitor, Tocris), 10 μM NU7441 (DNA-PK inhibitor, Tocris), or 10 μM VE-821 (ATR inhibitor, Sigma-Aldrich) for 1 hour, or with 10 μM SRPIN340 (SRPK1 inhibitor, MedChemExpress) for 48 hours.

Phos-tag gel analysis

For the detection of phosphorylated Y14, recombinant protein was denatured in Laemmli buffer (65 mM Tris, pH 6.8; 2% SDS; 10% glycerol; 5% 2-mercaptoethanol; 0.005% bromophenol blue) at 95 °C for 5 minutes, and resolved on a 12% SDS-polyacrylamide gel supplemented with 50 μM Phos-tag acrylamide AAL-107 (NARD Institute) and 100 μM $MnCl_2$. Electrophoresis was performed at a constant current of 25 mA per gel. Gels were stained using ToolStart Blue Staining Reagent (BIOTOOLS) to visualize protein bands.

doi:10.6342/NTU202502570

For samples treated with DDR kinase inhibitors, cell lysates were washed with TBS and solubilized in Laemmli buffer. Proteins were resolved on a 10% SDS-PAGE gel containing 35 μM Phos-tag acrylamide AAL-107 and 70 μM $ZnCl_2$ in Tris-MOPS running buffer (0.1 M Tris-base, 0.1 M MOPS, pH 7.8; 0.1% SDS; 5 mM $NaHSO_3$). Electrophoresis was conducted at 15 mA per gel for approximately 2.5 hours. Before transfer, gels were washed three times for 10 minutes in transfer buffer containing 25 mM Tris-base, 192 mM glycine, and 1 mM EDTA, followed by a single rinse in transfer buffer lacking EDTA. Proteins were transferred to pre-activated PVDF membranes using wet transfer in buffer containing 25 mM Tris-base, 192 mM glycine, and 10% methanol at 20 V for 18 hours. Membranes were blocked with 5% skim milk in TBST and probed with Y14-specific antibodies.

Protein purification of non-tagged Y14

The pET-GB1-Y14 plasmid was transformed into E. coli strain BL21 (DE3). Bacteria were grown at 37°C till OD_{600} reached 0.6. Recombinant protein expression was induced by 1 mM isopropyl β-d-1-thiogalactopyranoside (IPTG) at 25°C overnight. Bacteria were collected and cell pellet was resuspended in a buffer containing 50 mM Tris-HCl (pH 8.0), 750 mM NaCl, and 5% glycerol, and lysed using an N-2 NanoLyzer. The lysate was

doi:10.6342/NTU202502570

centrifuged at 12,000 × g for 30 minutes at 4°C. The supernatant was applied to a Ni-NTA resin column (GE Healthcare) and eluted with the above buffer containing 200 mM imidazole. The eluate was then dialyzed against a buffer containing 20 mM phosphate (pH 7) and 50 mM KCl, and subsequently loaded onto a HiPrep Heparin FF 16/10 column (GE Healthcare). The column was washed with a buffer containing 20 mM phosphate (pH 7) and 20 mM KCl. Elution was performed using a linear KCl gradient from 20 mM to 1 M in buffer. GB1-Y14 was eluted at approximately 0.55 M KCl. The eluate was dialyzed against a buffer containing 50 mM HEPES (pH 8), 100 mM KCl, and 1 mM DTT, and then treated with TEV protease overnight at 4°C. Ni-NTA affinity chromatography was used to remove the fusion tags. The flow-through was buffer-exchanged to a storage buffer containing 50 mM HEPES (pH 8) and 300 mM KCl. Purified recombinant Y14 was concentrated using an Amicon Ultra-15 device (Merck Millipore) and stored at -80°C.

In vitro phosphorylation of recombinant Y14

To study the effect of phosphorylated Y14 on phase separation, non-tagged recombinant Y14 and SRPK1 (MyBioSource) were mixed with a ratio of 60:1 (protein : kinase) by weight in kinase buffer containing 20 mM HEPES, pH7.9, 50 mM KCl, 2 mM $MgCl_2$, and 2 mM ATP at 30°C for 4 hr and let stand at RT for 1 hr. The phosphorylated Y14 was

doi:10.6342/NTU202502570

then changed to Y14 storage buffer (50 mM HEPES, 300 mM KCl, pH 8) and removed free ATP by PD SpinTrapTM G-25 (Cytiva) according to the manufacturer's instructions.

Mass Spectrometry

The *in vitro* phosphorylated recombinant Y14 was digested with Lys-C (1:20) using an in-solution digestion approach. After digestion, the samples were relatively quantified by LC-MS/MS, which was performed on a nanoACQUITY UPLC system (Waters, USA) coupled with an Orbitrap Exploris 480™ Hybrid Mass Spectrometer (Thermo Scientific, USA). MS raw files were processed using the built-in Sequest HT search engine and searched against the Human reference proteome (Uniprot, Taxonomy 9606, accessed June 12, 2024) in Proteome Discoverer (v.3.1., Thermo Fisher Scientific).

Liquid-liquid phase separation assay

Recombinant Y14 (in general 20 μM at final) was added to a buffer containing 20 mM HEPES (pH 7.2) and 50 mM KCl, followed by incubation at room temperature for 20 minutes to allow droplet formation. For LLPS of phosphor-Y14 (pY14), $MgCl_2$ (2.5 mM at the final concentration) and polyethylene glycol (PEG6000, 3% at the final concentration) were added alone or together to the protein samples. For heterotypic phase

doi:10.6342/NTU202502570

separation assays, pY14 was co-incubated with 0.5 μM Alexa Fluor 488-labeled Ku70/80, 0.2 μM Cy5-labeled *HOTAIRM1* or U25 RNA, or 0.2 μM Cy5-labeled dsDNA to assess condensate formation. Droplets were visualized on cover glasses for 30 minutes at 25 °C using Leica microscopy.

Blunt-end dsDNA was prepared by annealing the following oligonucleotides:

5'- GAT/iCy3/CCTGTCACGTGCTAGACTACTGGTCAACTCCATCAAGTAAGATG CAGATACTTAACGGCTCACAGAG-3
5'- CTCTGTGAGCCGTTAAGTATCTGCATCTTACTTGATGGAGTTGACCAGTAGT CTAGCACGTGACAGGATCCT-3'

Sedimentation assay

To evaluate condensate formation, 20 μl of Y14, Y14-ΔC, and pY14 at 20 μM was incubated at room temperature for 30 min to allow droplet formation. Samples were then centrifuged at 16,000 g for 45 min. After centrifugation, the upper and lower 10 μl fractions were collected and analyzed by SDS-PAGE.

Turbidity assay

To evaluate droplet formation, 10 μl of LLPS samples were incubated at room temperature for 30 minutes and subsequently assessed for turbidity by measuring optical

doi:10.6342/NTU202502570

density (OD) at 340 nm using a NanoDrop ND-1000 spectrophotometer (Thermo Fisher Scientific). A buffer containing 20 mM HEPES (pH 7.2) and 50 mM KCl was used as the blank control.

Fluorescence recovery after photobleaching (FRAP)

FRAP measurements were conducted on an inverted confocal microscope (LSM 780, Carl Zeiss) using a 100×1.4 oil-immersion objective (Plan-Apochromat DIC M27). 0.5 μM of Alexa Fluor 488-labeled Y14 or pY14 was combined with 20 μM of unlabeled protein in LLPS buffer containing Mg^{2+} and PEG, followed by incubation in confocal dishes (SPL Life Sciences) at room temperature for 30 min. Droplets ranging from 7–30 μm^2 were selected, and photobleaching was applied to a defined ROI (1.22 μm^2, <20% of the droplet area) using a 488 nm laser at full intensity. Time-lapse acquisition was performed at 10-sec intervals over 200 sec. A minimum of five droplets across three independent experiments were analyzed. Fluorescence recovery dynamics were quantified with ZEN (Black Edition) software, and normalized recovery was calculated using the formula: $\frac{I_{bleach}(t)-I_b}{I_{non-bleach}(t)-I_b}$, where I_{bleach}, $I_{non\text{-}bleach}$, and I_b represent fluorescence intensities within the bleached and reference regions, respectively, and I_b denotes background signal.

doi:10.6342/NTU202502570

Far Western

Recombinant pY14 protein (2 μg) was separated on a 12% native polyacrylamide gel using a running buffer composed of 25 mM Tris-HCl and 100 mM glycine (pH 8.9), followed by transfer onto a nitrocellulose membrane (Amersham™, GE Healthcare). After staining the membrane with Ponceau S, the region corresponding to pY14 was excised and blocked in TBST supplemented with 5% BSA (100 mM Tris-base, pH 7.6, 154 mM NaCl, 0.1% Tween-20) for 30 minutes at room temperature. The membrane was subsequently washed and incubated with 30 or 60 ng of TAMRA-labeled IDR peptides diluted in 1 ml of HEPES buffer (20 mM HEPES, 50 mM KCl, pH 7.2) at room temperature for 30 minutes. After three washes with TBS (100 mM Tris-HCl, pH 7.6, 154 mM NaCl), fluorescence signals were captured using the Alexa Fluor 555 channel on the iBright™ FL1500 Imaging System. Signal quantification was performed with ImageJ by selecting equal-sized regions of interest (ROI) across membranes.

PAR binding assay

To examine interactions between poly(ADP-ribose) and Y14 proteins, biotin-conjugated PAR polymer (R&D Systems) was incubated with 1 μM recombinant Y14, pY14, and

doi:10.6342/NTU202502570

Y14-ΔC. Reactions were carried out in NETN buffer (50 mM Tris-HCl, pH 8.0; 100 mM NaCl; 0.5 mM EDTA; 0.5% NP-40) supplemented with protease inhibitors (Roche) for 2 hours at room temperature. Complexes were captured using magnetic streptavidin beads (Thermo Fisher Scientific), washed, and analyzed by immunoblotting with antibodies targeting Y14. To assess enrichment levels, 5% of each input sample was loaded as a reference control.\

***In vitro* transcription**

As previously described [81], the pGEM-T vector encoding the HOTAIRM1 fragment (396–631 nt) was linearized with NotI (New England Biolabs), followed by phenol-chloroform extraction (PCA) and ethanol precipitation. The linearized DNA was used as a template for in vitro transcription with T7 RNA Polymerase (Promega) at 37 °C for 2 hours. The transcription reaction contained 500 μM CTP and GTP, 100 μM UTP, 0.3 μM [α-^{32}P] UTP (3000 Ci/mmol, PK-BLU507H, PerkinElmer), and a total of 500 μM of ATP and m^{6}ATP (N-1013, TriLink biotechnologies) at the indicated ratios. After the transcription, RQ1 (M6101, Promega) was added at 37 °C for 15 min to remove the DNA template. Unincorporated isotopes were removed using MicroSpin G-25 columns (GE Healthcare) by centrifugation at 3000 rpm according to the manufacturer's instructions.

doi:10.6342/NTU202502570

The specific radioactivity of transcribed HM1-3 was approximately 2.4×10^6 cpm/μg, and the transcript was analyzed on a 6% RNA sequencing gel and used for subsequent assays.

For in vitro transcription of m6A oligos, oligos listed in Table 1 were first annealed with the T7 promoter to synthesize the hybridized templates. The oligo and T7 promoter mixture in the transcription buffer (P1181, Promega) was heated at 95°C for 2 min and then gradually cooled by decreasing 8°C every 5 min to a final 25°C. The hybridized templates (0.7 μg) were used for in vitro transcription with T7 RNA Polymerase (Promega) at 37 °C for 4 hours, each reaction contains 0.4 mM m6ATP, 2 mM UTP, 1 mM GTP and CTP. RQ1 was further treated to digest the hybridized templates and followed by PCA extraction and ethanol precipitation. For end-labeling of the transcripts, the γ-phosphate of RNAs was removed by 5 μl of alkaline phosphatase (Merck, 11097075001) treatment for every 100 pmol of RNA at 50 °C for 1 hr, followed by PCA extraction. The purified RNA was then end-labeled with [γ-^{32}P] ATP (6000 Ci/mmol, PK-BLU502Z, PerkinElmer) by T4 polynucleotide kinase (T4 PNK, M0201S, New England Biolabs) in the T4 PNK reaction buffer, incubated at 37 °C for 1 hr. The free nucleotides, including [γ-^{32}P] ATP, were removed by MicroSpin G-25 columns according to the manufacturer's instructions.

doi:10.6342/NTU202502570

The specific radioactivity of transcribed oligo was approximately 2.7×10^7 cpm/μg, and the transcript was analyzed on a 6% RNA sequencing gel and used for subsequent assays.

Electrophoretic Mobility Shift Assay (EMSA)

Radiolabeled RNA probes, including ^{32}P-labeled *HOTAIRM1* fragment 3 (148-183 fM) and ^{32}P-labeled m^{6}A oligonucleotides (112–174 fM), were incubated with indicated concentration of recombinant Y14 protein in binding buffer containing 50 mM HEPES (pH 7.0), 150 mM NaCl, 1 mM DTT, 10% glycerol, and 0.5 mg/mL BSA. The reactions were carried out on ice for 20 minutes. After incubation, samples were mixed with loading dye (0.01% xylene cyanol and 0.01% bromophenol blue) and resolved on 4% (for HOTAIRM1 fragment 3, 1044 nt) or 8% (for ^{6}A oligos) native polyacrylamide gels using Tris-Borate-EDTA buffer. Gels were then vacuum-dried and visualized with a Typhoon phosphorimager (GE Healthcare). Signal intensities were quantified using ImageQuant TL software (GE Healthcare), and dissociation constants (Kd) were derived from the probe concentrations at which 50% of RNA was bound by Y14.

doi:10.6342/NTU202502570

Figures

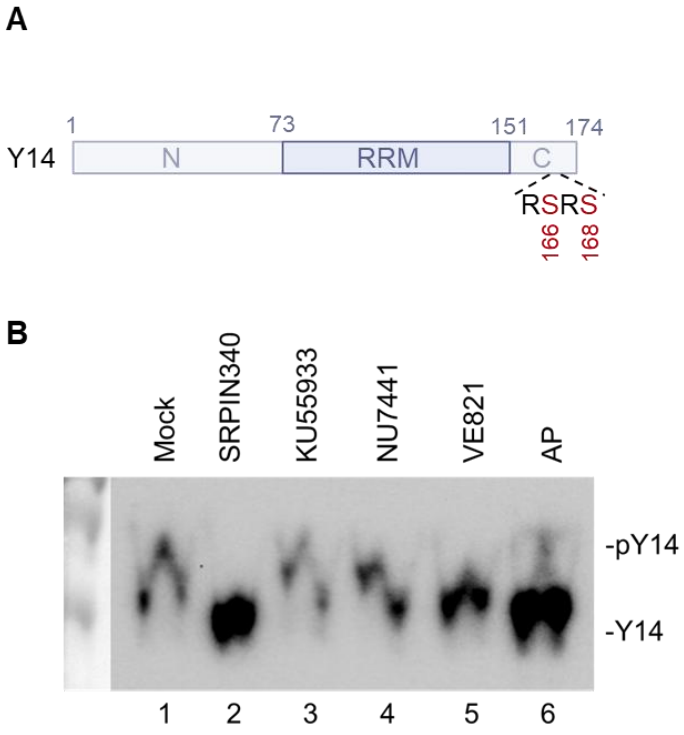

Fig. 1 SRPK1 phosphorylates Y14 *in vivo*

(A) Schematic representation illustrating the phosphorylation sites within the RS dipeptides of Y14. (B) U2OS cells were either mock-treated (lanes 1 and 6) or treated with SRPIN340 (SRPK1 inhibitor, lane 2), KU55933 (ATM inhibitor, lane 3), NU7441 (DNA-PK inhibitor, lane 4), or VE821 (ATR inhibitor, lane 5). For mock lysates, alkaline phosphatase (AP) treatment was applied in lane 6 to confirm phosphorylation-dependent mobility shift. Cell lysates were resolved on Zn^{2+}-Phos-tag SDS-PAGE and immunoblotted with a Y14 antibody.

doi:10.6342/NTU202502570

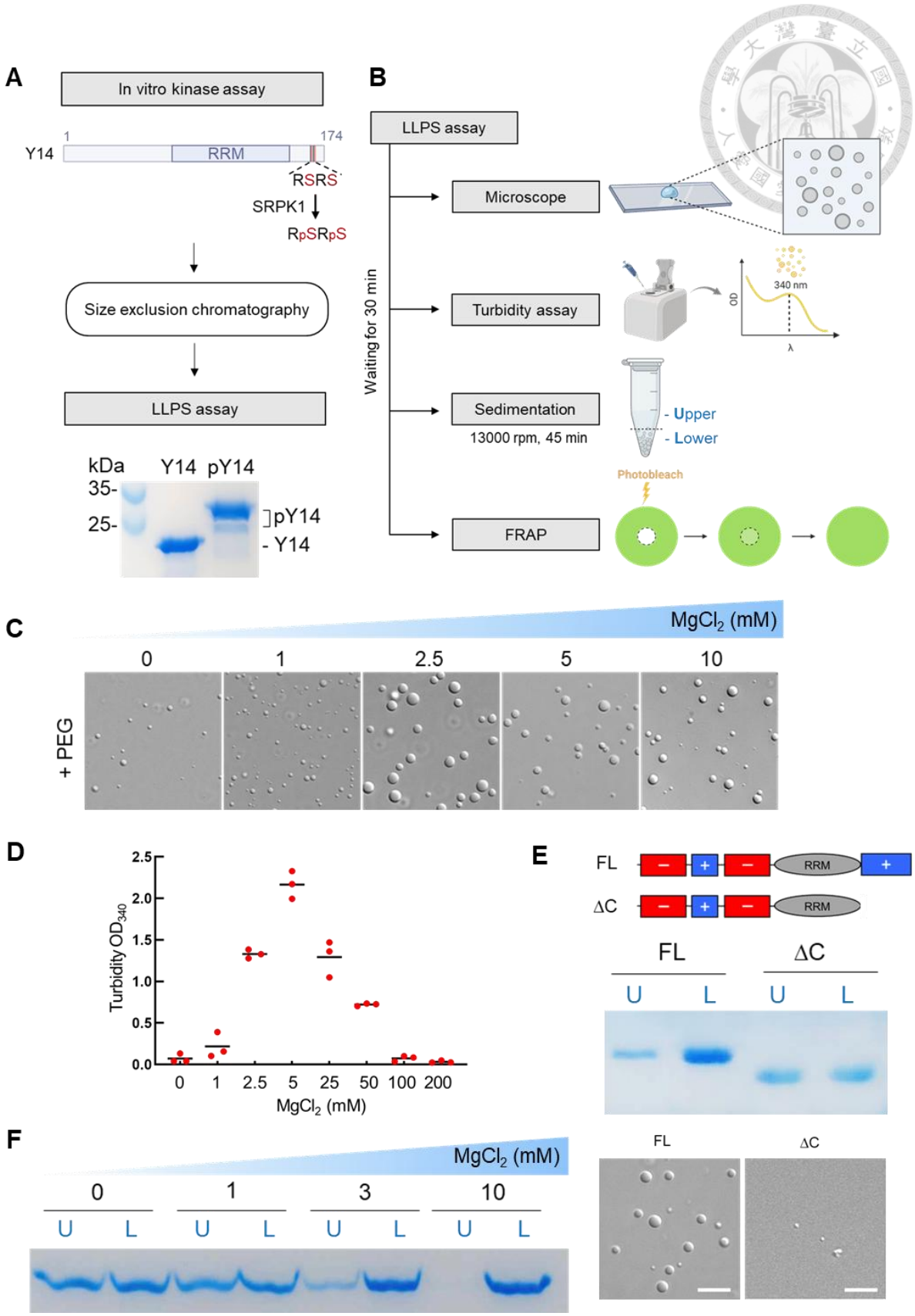

doi:10.6342/NTU202502570

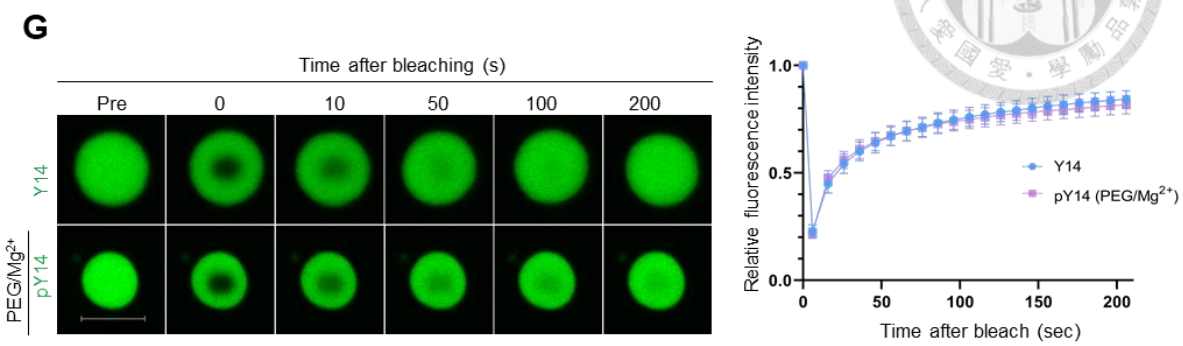

Fig. 2 Mg^{2+} promotes LLPS of pY14

(A) *In vitro* kinase assay for Y14 phosphorylation. Y14 was phosphorylated by SRPK1, followed by buffer exchange for protein storage using size exclusion chromatography. The resulting protein was then subjected to the LLPS assay. (B) LLPS assay was performed prior to subsequent analyses, including microscopy imaging, turbidity measurement, sedimentation assay, and fluorescence recovery after photobleaching (FRAP) assay. (C) Representative images showing pY14 droplet formation under varying Mg^{2+} concentrations in the presence of 3% PEG. Scale bar: 10 μm. (D) Statistical analysis of the turbidity assay. Optical density at 340 nm (OD_{340}) was measured following pY14 droplet formation in the presence of 3% PEG under the indicated Mg^{2+} concentrations (mean ± SD; n=3). (E) Sedimentation assay comparing the phase separation ability of full-length Y14 (Y14-FL) and C-terminal deletion Y14-DC under titrated Mg^{2+}

doi:10.6342/NTU202502570

concentrations. Phase-separated droplets were centrifuged, and the upper and lower fractions were collected for SDS-PAGE analysis and quantification. Proteins were stained with Coomassie Blue. The schematic structures of Y14-FL and Y14-DC are shown. Representative images showing droplet formation of Y14-FL and Y14-DC. Scale bar: 10 μm. (F) Sedimentation assay of pY14 in the presence of PEG under titrated Mg^{2+} concentrations. (G) Fluorescence recovery kinetics of Y14 and pY14 (Mg^{2+}/PEG) droplets analyzed by FRAP assay. The fluorescence images depict recovery following photobleaching, while quantitative analysis illustrates the recovery dynamics over time. Scale bar: 5 μm. Panels C, E (LLPS assay), and G were reproduced from Hsin-Hong Yeh's results.

doi:10.6342/NTU202502570

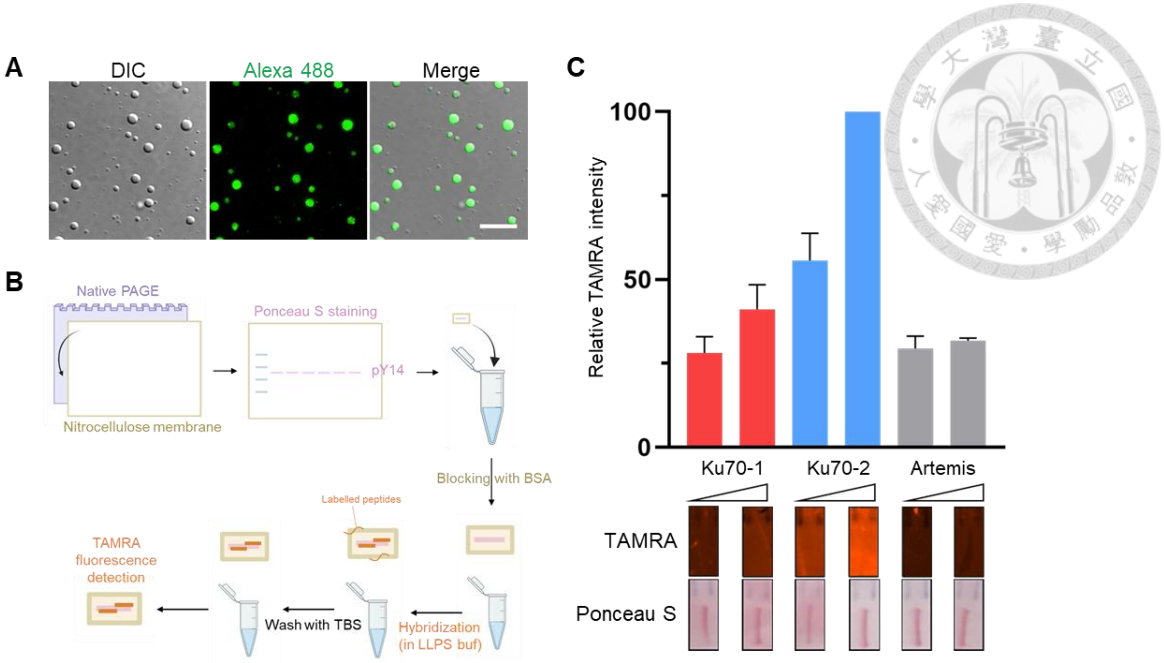

Fig. 3 Analysis of the interaction between pY14 and IDR peptides using Far Western blot

(A) Representative DIC and fluorescence images showed the co-phase separation of Alexa Fluor 488-labeled Ku70/80 with pY14. Scale bar: 10 μm. Reproduced from Hsin-Hong Yeh's result. (B) Schematic workflow of Far Western analysis. Recombinant pY14 was resolved by native PAGE, transferred to a nitrocellulose (NC) membrane, and incubated with 30 or 60 ng of TAMRA-labeled IDR peptides. Interaction was detected via the Alexa555 fluorescence channel. (C) Quantification of TAMRA fluorescence intensity from four independent experiments (mean ± SD; N=4). Ponceau S staining confirmed equal protein loading.

doi:10.6342/NTU202502570

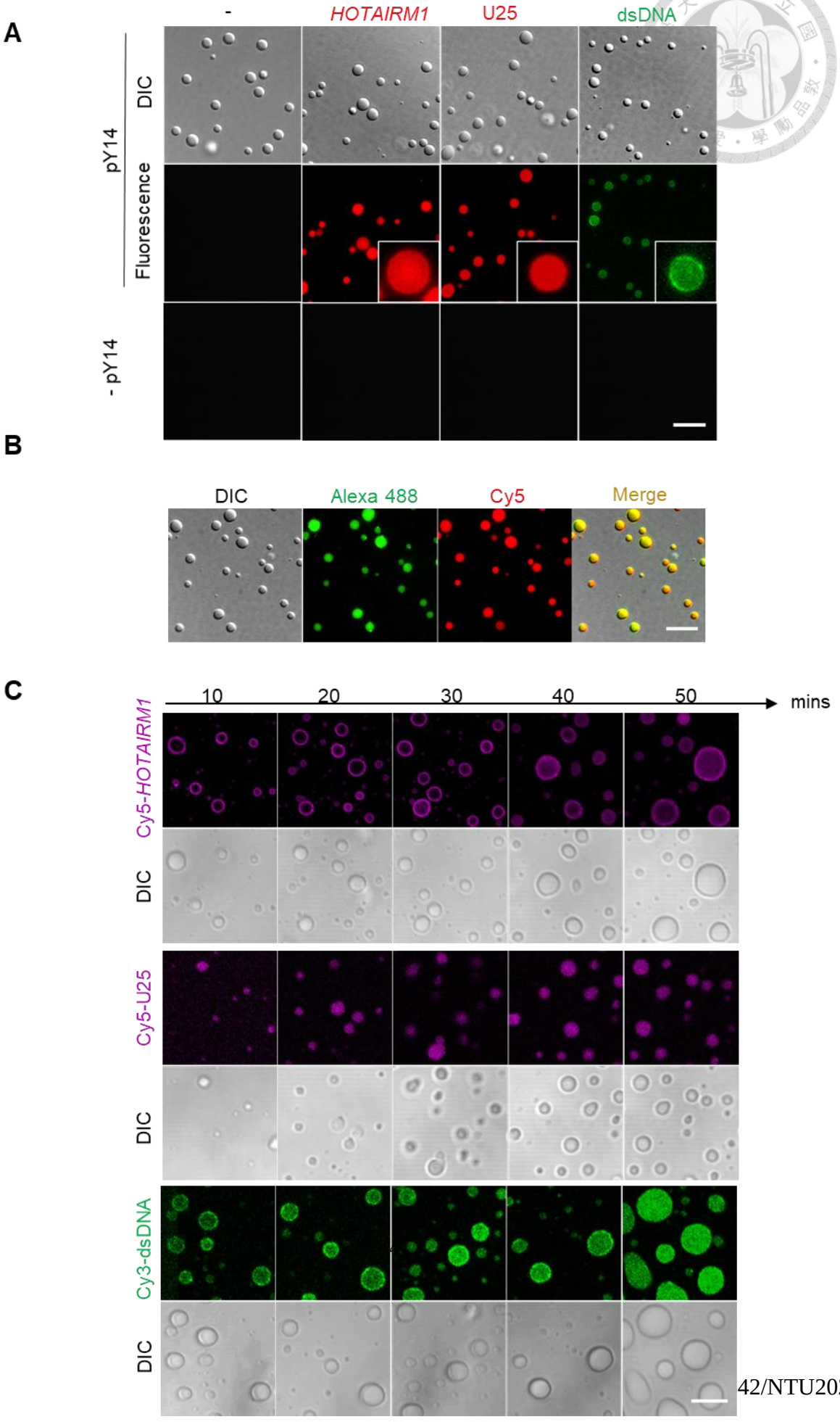
A
-
HOTAIRM1
U25
dsDNA
pY14
DIC
Fluorescence
- pY14
B
DIC
Alexa 488
Cy5
Merge
C
10
20
30
40
50
mins
Cy5-HOTAIRM1
DIC
Cy5-U25
DIC
Cy3-dsDNA
DIC

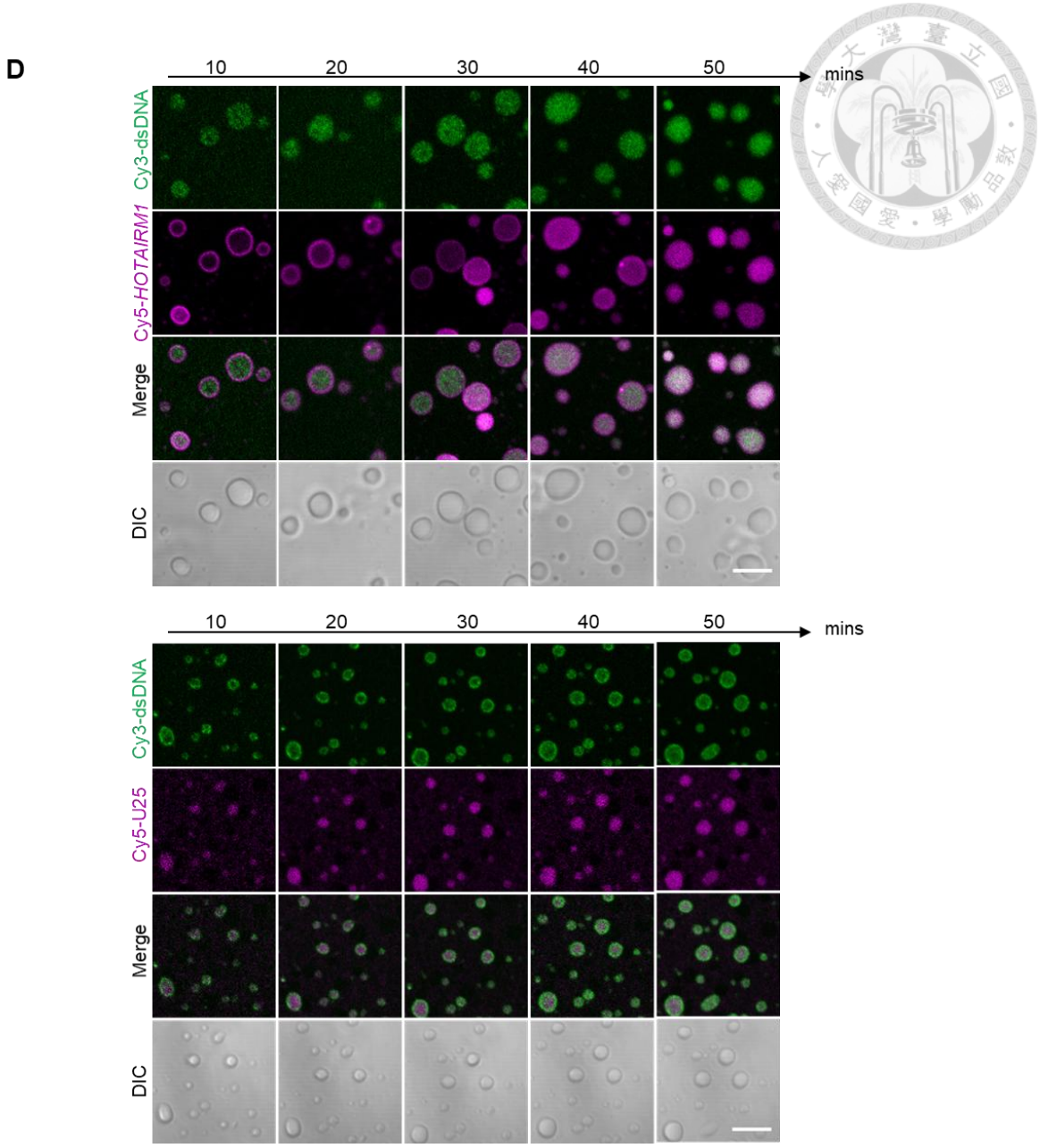

Fig. 4 Co-phase separation of nucleic acids with pY14

(A) Cy5-labeled *HOTAIRM1* and U25 (red), or Cy3-labeled dsDNA (green), were co-incubated with pY14 in the presence of Mg^{2+} and PEG. Representative DIC and fluorescence images illustrate nucleic acid enrichment within pY14 droplets. Magnified

doi:10.6342/NTU202502570

views are shown in the insets. Scale bar: 10 μm. (B) Co-phase separation of Cy5-*HOTAIRM1* and Alexa Fluor 488-labeled Ku70/80 with pY14. Fluorescence signals reveal co-localization within condensates. Scale bar: 10 μm. (C) Time-lapse confocal microscopy monitoring droplet formation over 0–50 minutes for individual nucleic acids (Cy5-*HOTAIRM1*, Cy5-U25, or Cy3-dsDNA) co-incubated with pY14. (D) Partitioning dynamics of Cy5-HOTAIRM1 or Cy5-U25 into pY14 droplets in the presence of Cy3-dsDNA, assessed over the same 50-minute time window by confocal imaging. Scale bar in (A, C, and D): 5 μm.

doi:10.6342/NTU202502570

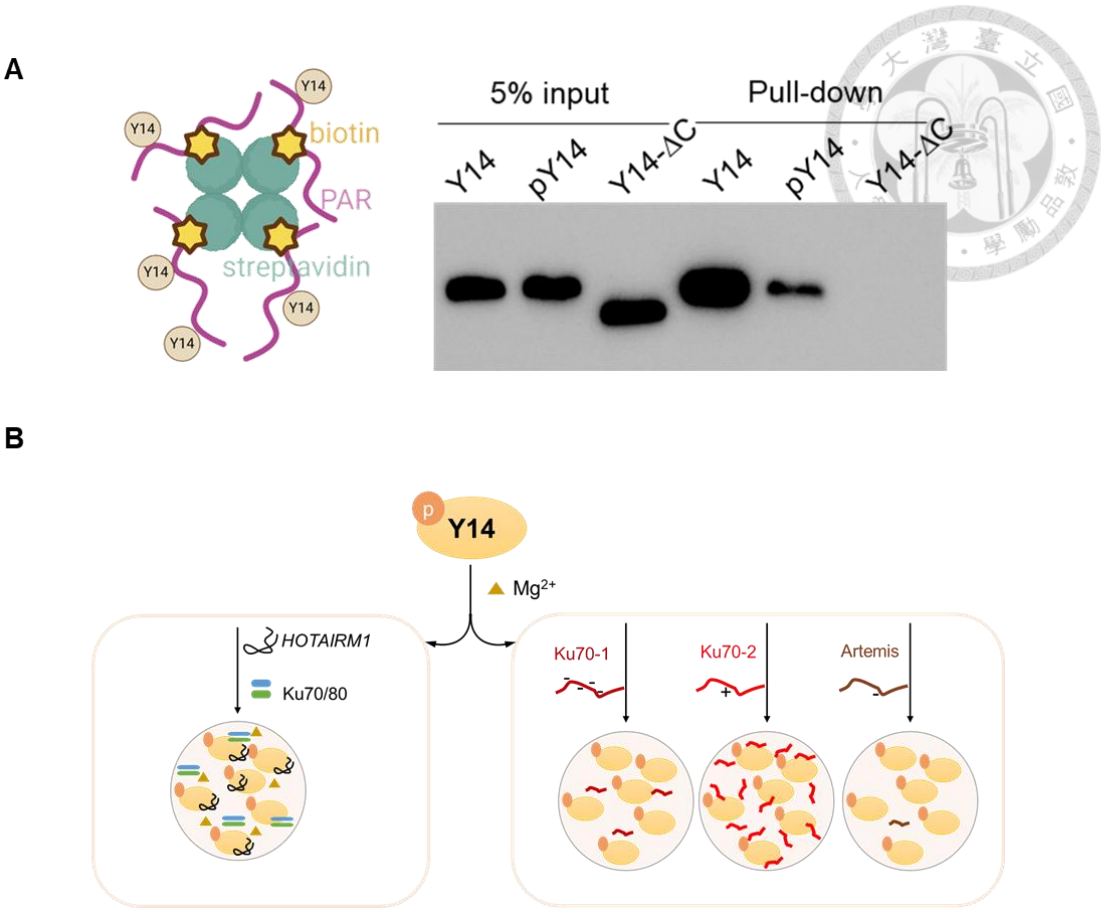

Fig. 5 Y14 interacts with PAR

(A) PAR binding assay using 1 μM of recombinant Y14, pY14, or Y14-ΔC incubated with 1 μM of biotin-labelled PAR, followed by pull-down by streptavidin. Reproduced from Tzu-Wei Chung's result. (B) Model of Mg^{2+} promoted pY14-driven phase separation. lncRNA *HORAIRM1* and NHEJ factors Ku70/80 co-phase separated with pY14. On the other hand, positively charged IDR peptides portioned into pY14 droplets more efficiently.

doi:10.6342/NTU202502570

Appendix

A

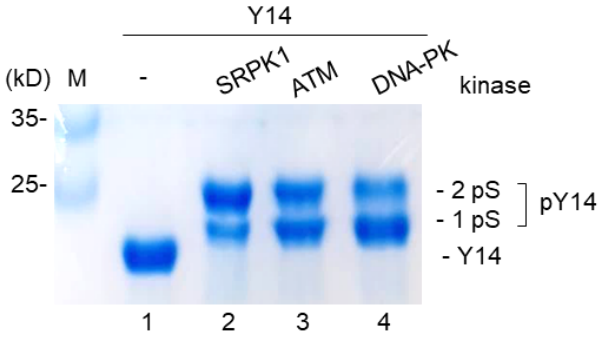

B

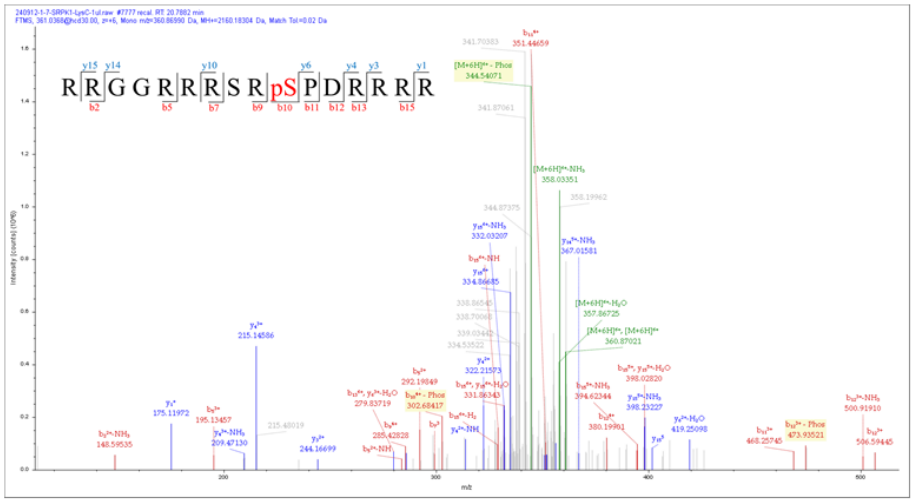

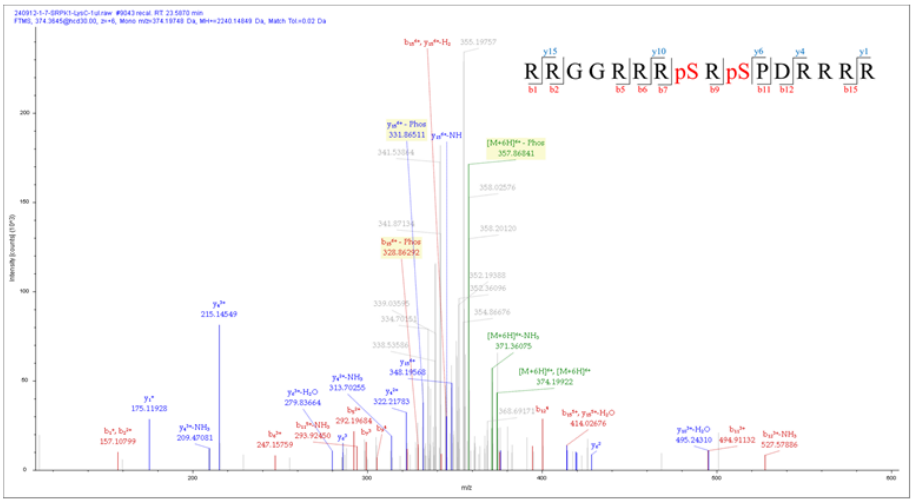

doi:10.6342/NTU202502570

C

		SRPK1	ATM	DNA-PK
Annotated Sequence	Modifications	PSM		
[K].RRGGRR**R**S**R**S**S**PDRRRR.[-]	1xPhospho [S]	30	8	83
[K].RRGGRR**R**S**R**S**S**PDRRRR.[-]	2xPhospho [S8(100); S10(100)]	64	8	60

Appendix 1 *In vitro* phosphorylation of Y14

(A) *In vitro* phosphorylation of pY14 by recombinant SRPK1, ATM and DNA-PK. Phosphorylated Y14 was analyzed using Mn^{2+}-Phos-tag SDS-PAGE and stained with Coomassie Blue. (B) Annotated sequences and modification sites of pY14-derived peptides identified by mass spectrometry. The table presents two peptides with distinct phosphorylation patterns. [K] denotes the Lys-C enzymatic cleavage site. Peptide-spectrum matches (PSMs) were filtered at 1% FDR to ensure identification reliability. (C) Mass spectra of the two phosphorylated peptides in (B), showing either one (up) or two (down) 79.96 Da shifts, corresponding to phospho-serine modifications.

doi:10.6342/NTU202502570

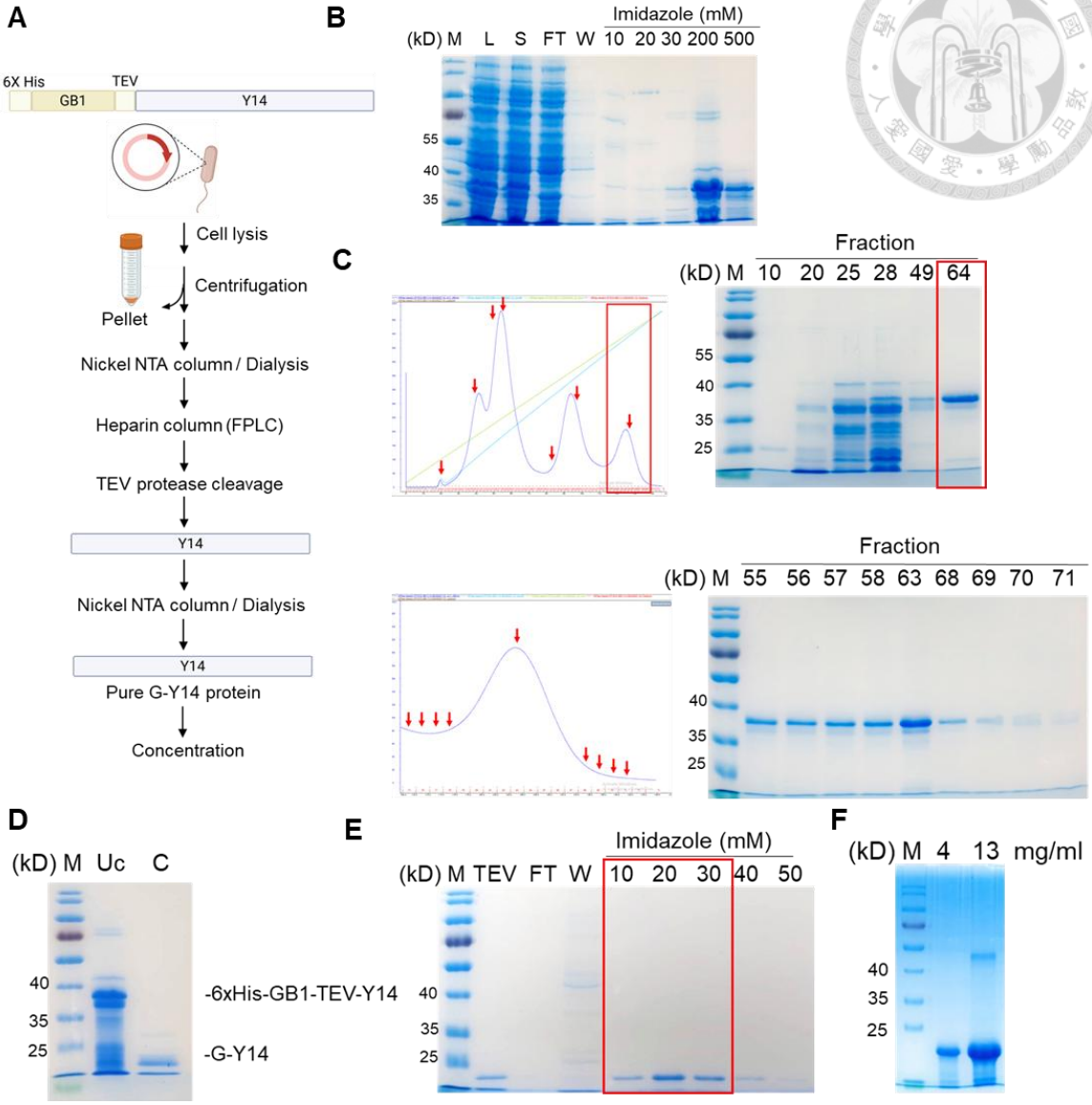

Appendix 2 Non-tagged recombinant Y14 purification

(A) Procedure for non-tagged recombinant Y14 purification: Competent BL21 cells expressing His-GB1-Y14 were lysed and loaded onto a Ni-NTA column, followed by elution with 200 mM imidazole (B). The His-tagged Y14 was fractionated by fast protein

doi:10.6342/NTU202502570

liquid chromatography (FPLC) (C), and the His-tag was cleaved using TEV protease (D). The resulting non-tagged Y14 was purified by an additional Ni-NTA chromatography step, eluted with 10–30 mM imidazole (E), then dialyzed in storage buffer and concentrated.

doi:10.6342/NTU202502570

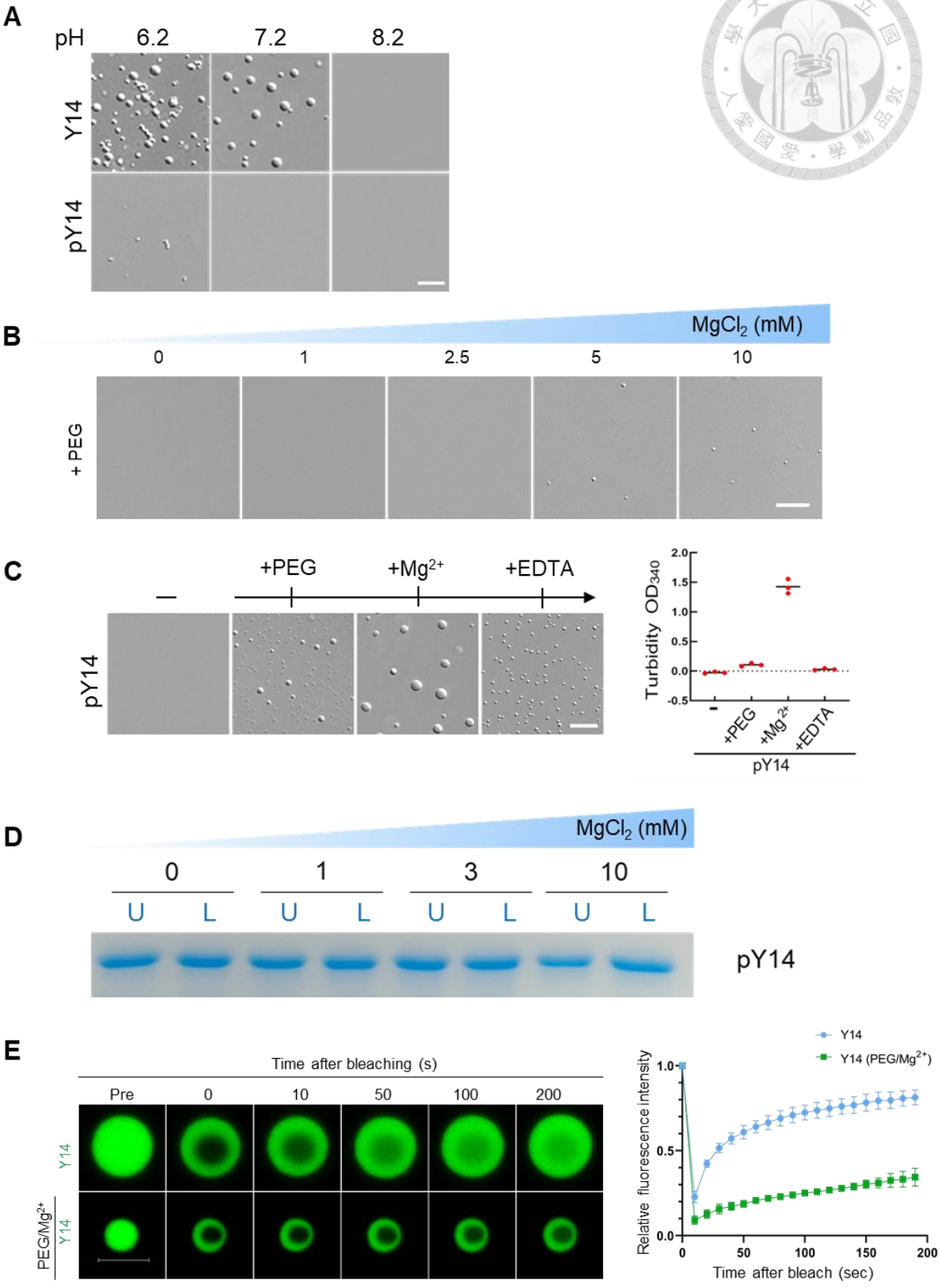

doi:10.6342/NTU202502570

Appendix 3 Mg^{2+} promotes LLPS of pY14

(A) Representative images of Y14 and pY14 droplet formation under varying pH conditions. (Scale bar: 10 μm.) (B) Representative images showing pY14 droplet formation under varying Mg^{2+} concentrations in the absence of 3% PEG. (Scale bar: 10 μm.) (C) Representative images showing turbidity assay measuring phase separation of pY14 following sequential addition of PEG, Mg^{2+}, and EDTA. Optical density at 340 nm (OD_{340}) was recorded to assess turbidity changes. (Scale bar: 10 μm.) (D) Sedimentation assay of pY14 in the absence of PEG under titrated Mg^{2+} concentrations. (E) Fluorescence recovery kinetics of Y14 droplets analyzed by FRAP assay in the presence or absence of Mg^{2+}/PEG. The fluorescence images depict recovery following photobleaching, while quantitative analysis illustrates the recovery dynamics over time. (Scale bar: 5 μm.) Except for panel D, all panels were reproduced from Hsin-Hong Yeh's results.

doi:10.6342/NTU202502570

A

	FCR	f-	f+	NCPR
Y14-1 (1-70)	0.457	0.286	0.200	-0.114
Y14-2 (151-174)	0.583	0.042	0.542	0.500
Ku70-1 (1-28)	0.429	0.393	0.036	-0.357
Ku70-2 (536-562)	0.481	0.222	0.296	0.037
Ku80-1 (543-594)	0.235	0.137	0.137	-0.039
Ku80-2 (705-732)	0.370	0.296	0.074	-0.222
DNA-PK-1 (2050-2073)	0.375	0.125	0.250	0.125
DNA-PK-2 (3200-3225)	0.423	0.385	0.038	-0.346
artemis (363-692)	0.282	0.179	0.127	-0.076
artemis-peptide (529-550)	0.045	0.045	0.091	-0.045
XRCC4-1 (212-249)	0.324	0.297	0.027	-0.270
XRCC4-2 (264-336)	0.361	0.194	0.181	-0.028
PARP1-1 (198-233)	0.600	0.257	0.343	0.086
PARP1-2 (361-385)	0.000	0.000	0.000	0.000
53BP1-1 (24-273)	0.272	0.200	0.100	-0.128
53BP1-2 (742-911)	0.324	0.235	0.100	-0.147
53BP1-3 (1269-1478)	0.248	0.129	0.129	-0.010
MRE11-1 (507-540)	0.477	0.273	0.205	-0.068
MRE11-2 (556-614)	0.305	0.085	0.220	0.136
MRE11-3 (651-708)	0.345	0.207	0.138	-0.069
NBS1-1 (326-346)	0.048	0.000	0.095	0.048
NBS1-2 (396-415)	0.200	0.100	0.100	0.000
NBS1-3 (430-478)	0.306	0.122	0.184	0.061

B

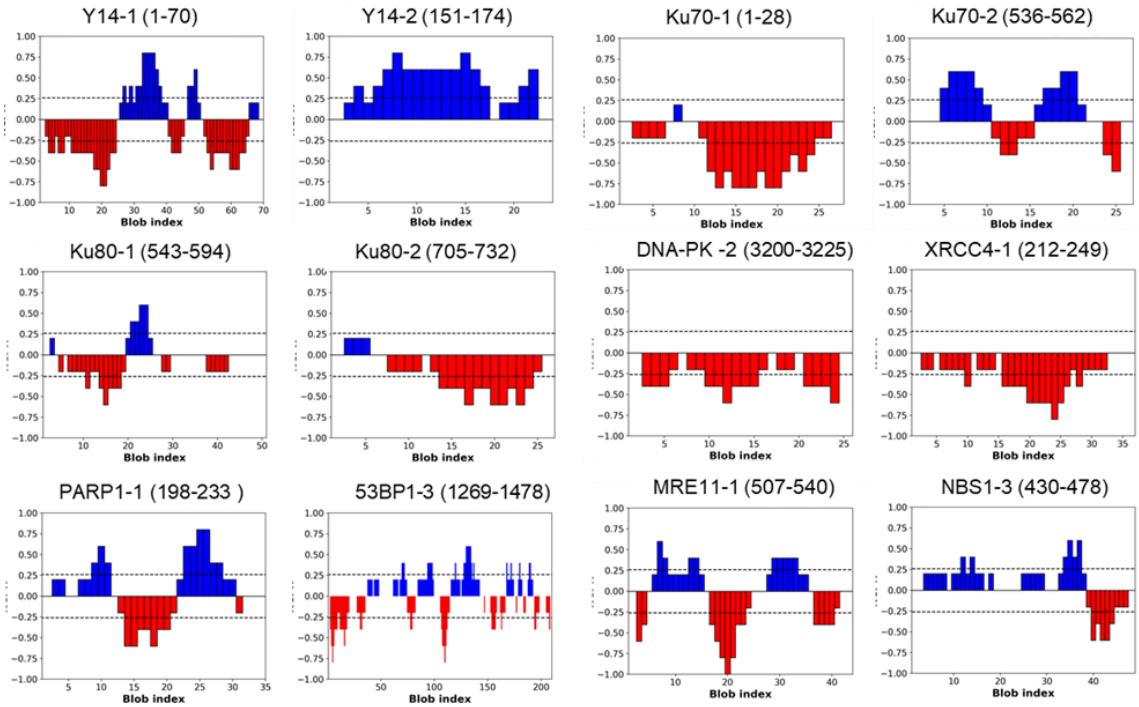

doi:10.6342/NTU202502570

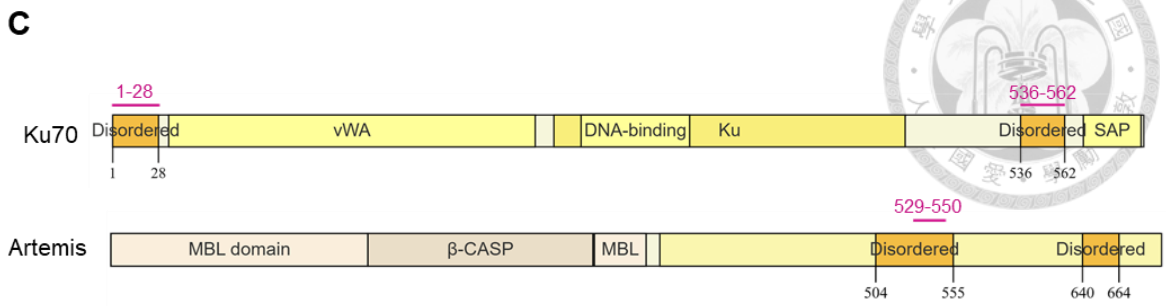

Peptides	Amino acid sequence	Length	NCPR
Ku70-1	MSGWESYYKTEGDEEAEEEQEENLEASG	28	-0.357
Ku70-2	PEGKVTKRKHDNEGSGSKRPKVEYSEE	27	0.037
Artemis	STHISSQNSSQSTHITEQGSQG	22	-0.045

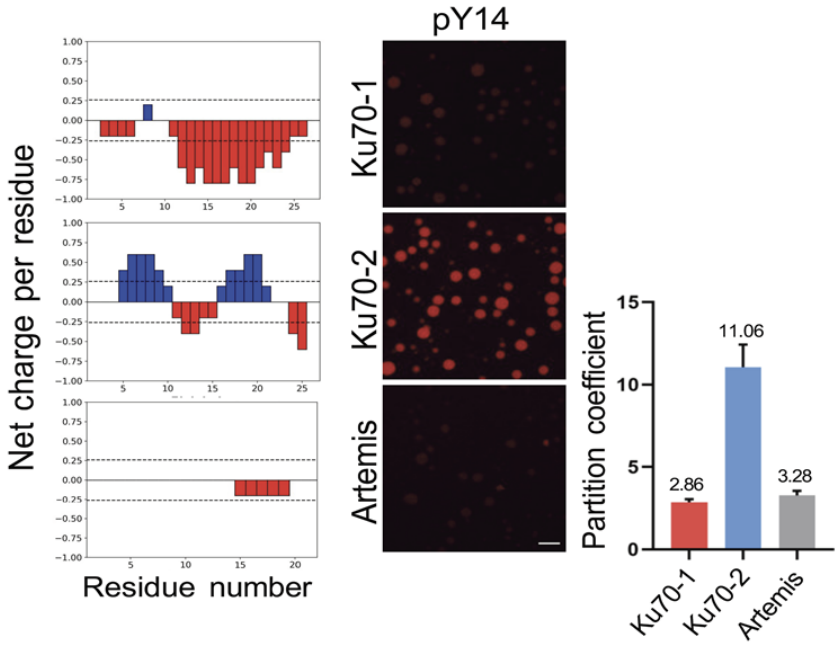

Appendix 4 Electrostatic interaction drives Ku70 partitioning into pY14 condensates

(A) Bioinformatic analysis of DDR factors containing charged intrinsically disordered

doi:10.6342/NTU202502570

regions (IDRs), including fraction of charged residues (FCR), fractions of positively (f^+) and negatively (f^-) charged residues, and net charge per residue (NCPR). (B) Distribution of NCPR values across the charged IDRs of DDR factors. (C) Top: Schematic diagrams showing IDRs and peptide design for Ku70 and Artemis. Middle: Amino acid sequences and corresponding NCPR values of Ku70-1, Ku70-2, and Artemis peptides (table provided by Chiu-Lun Shen; manuscript under revision). Bottom: Partition coefficient analysis and NCPR plot illustrating differential partitioning behaviors of Ku70-1 (negatively charged), Ku70-2 (net positive charge), and Artemis (containing only a single basic residue). 2 μM of TAMRA-labeled peptides were co-incubated with 20 μM of pY14 in the presence of Mg^{2+} and PEG. Phase separation was visualized using laser-scanning confocal microscopy. (Scale bar: 10 μm.) Panel C was reproduced from Hsin-Hong Yeh's result.

doi:10.6342/NTU202502570

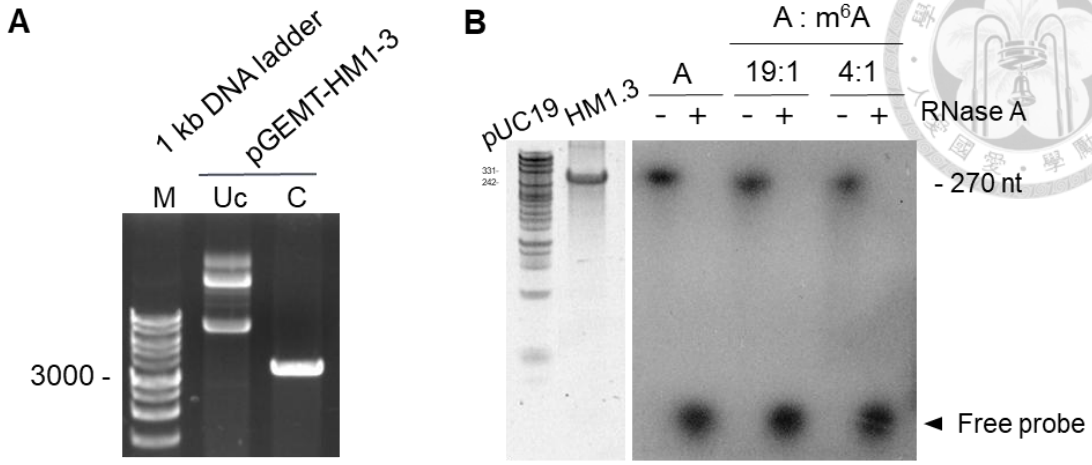

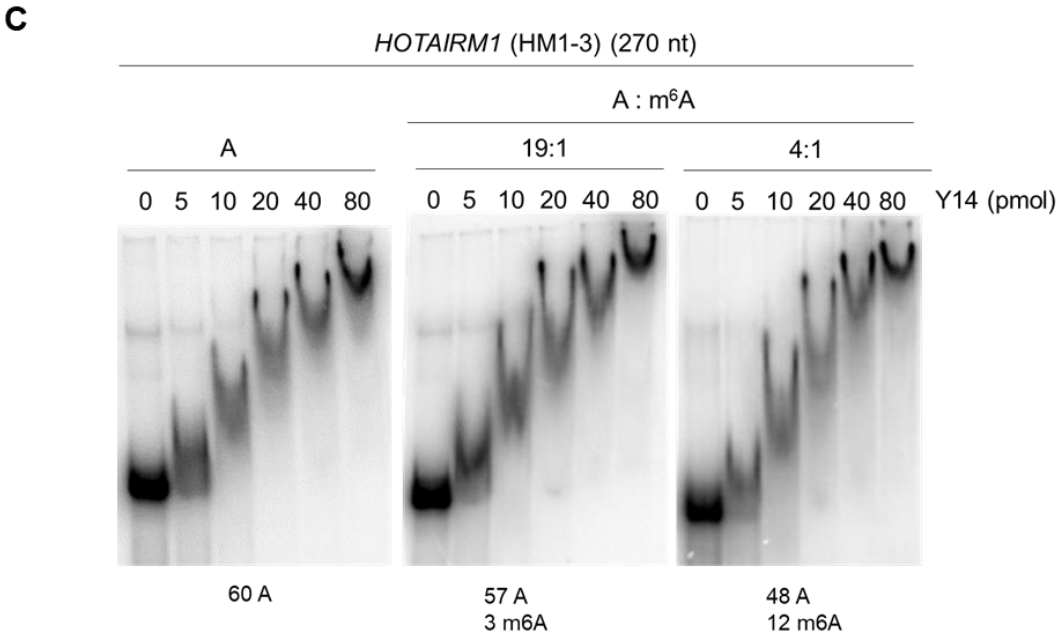

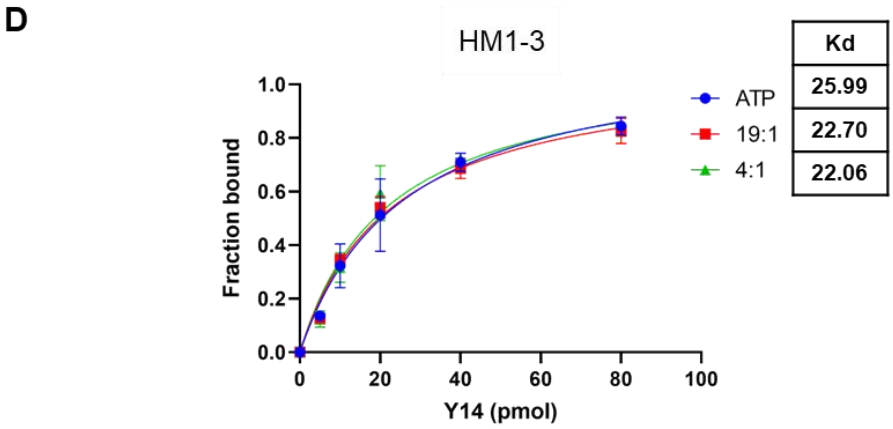

doi:10.6342/NTU202502570

Appendix 5 EMSA shows that m^{6}A modification does not affect the binding between Y14 and lncRNA HM1-3

(A) The plasmid pGEMT-HM1-3 was linearized with NotI. (B) In vitro transcription of HM1-3 with indicated ATP:m^{6}ATP ratios, performed without isotope labeling (left) and with [α-^{32}P] UTP labeling (right). (C) Electrophoretic mobility shift assay (EMSA) was conducted using increasing amounts (0–80 pmol) of purified Y14 protein and differentially m^{6}A-modified HM1-3: 154 fmol of unmodified HM1-3, 183 fmol of HM1-3 with a 19:1 ATP:m^{6}ATP ratio, and 148 fmol with a 4:1 ratio. (D) Binding fractions were quantified (n=3), and dissociation constants (Kd) were calculated.

doi:10.6342/NTU202502570

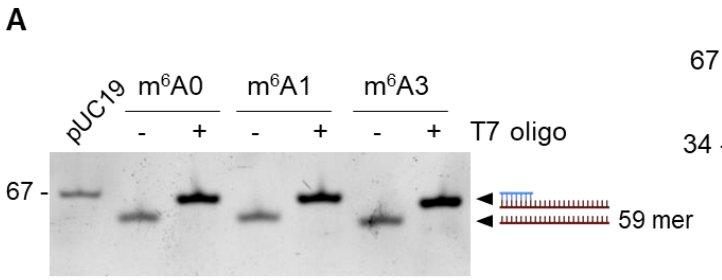

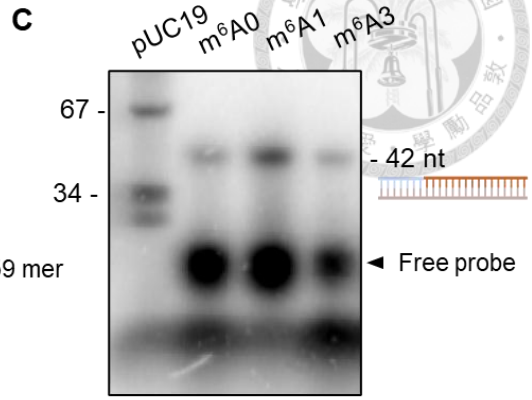

B

RNA: 42 mer [in vitro transcribed]

m^{6}A3	GGUUGGACUUUUGGUCUUUUGGACUUUUGGUCUUUUGGACUU
m^{6}A1	GGUUGGUCUUUUGGUCUUUUGGACUUUUGGUCUUUUGGUCUU
m^{6}A0	GGUUGGUCUUUUGGUCUUUUGGUCUUUUGGUCUUUUGGUCUU

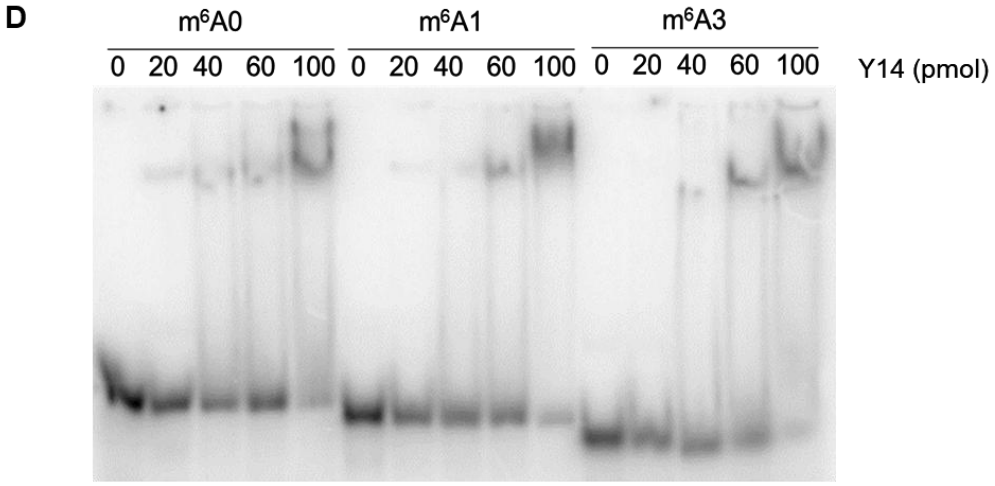

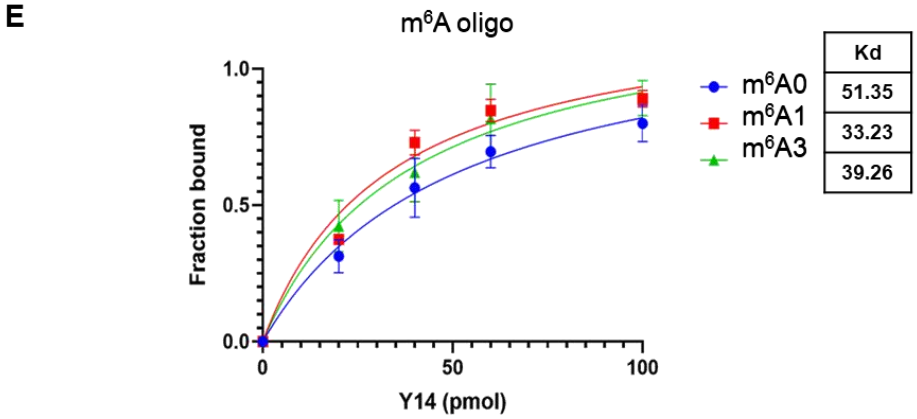

doi:10.6342/NTU202502570

Appendix 6 EMSA shows that m^{6}A modification does not affect Y14 and RNA binding

(A) Annealing of T7 promoter and m^{6}A oligos (Listed in B). (C) *In vitro* transcription of m^{6}A oligos with m^{6}ATP instead of ATP, followed by alkaline phosphatase treatment and [γ-^{32}P] ATP end-labeling. (D) Electrophoretic mobility shift assay (EMSA) was conducted using increasing amounts (0–80 pmol) of purified Y14 protein and differentially m^{6}A-modified oligos: 174 fmol of m^{6}A0, 112 fmol of m^{6}A1, and 123 fmol of m^{6}A3. (E) Binding fractions were quantified (n=3), and dissociation constants (Kd) were calculated.

doi:10.6342/NTU202502570

Reference

1. Lindahl, T., *Instability and decay of the primary structure of DNA.* Nature, 1993. **362**(6422): p. 709-715.
2. Aziz, K., et al., *Targeting DNA damage and repair: Embracing the pharmacological era for successful cancer therapy.* Pharmacology & Therapeutics, 2012. **133**(3): p. 334-350.
3. Huang, R. and P.-K. Zhou, *DNA damage repair: historical perspectives, mechanistic pathways and clinical translation for targeted cancer therapy.* Signal Transduction and Targeted Therapy, 2021. **6**(1): p. 254.
4. Ciccia, A. and S.J. Elledge, *The DNA Damage Response: Making It Safe to Play with Knives.* Molecular Cell, 2010. **40**(2): p. 179-204.
5. Bi, X., *Mechanism of DNA damage tolerance.* World J Biol Chem, 2015. **6**(3): p. 48-56.
6. Chao, H.X., et al., *Orchestration of DNA Damage Checkpoint Dynamics across the Human Cell Cycle.* Cell Systems, 2017. **5**(5): p. 445-459.e5.
7. Abraham, R.T., *Cell cycle checkpoint signaling through the ATM and ATR kinases.* Genes Dev, 2001. **15**(17): p. 2177-96.
8. Lagerwerf, S., et al., *DNA damage response and transcription.* DNA Repair, 2011. **10**(7): p. 743-750.
9. Ghosal, G. and J. Chen, *DNA damage tolerance: a double-edged sword guarding the genome.* Transl Cancer Res, 2013. **2**(3): p. 107-129.
10. Scully, R., et al., *DNA double-strand break repair-pathway choice in somatic mammalian cells.* Nature Reviews Molecular Cell Biology, 2019. **20**(11): p. 698-714.
11. Castedo, M., A. Lafarge, and G. Kroemer, *Poly(ADP-ribose) polymerase-1 and its ambiguous role in cellular life and death.* Cell Stress, 2023. **7**(1): p. 1-6.
12. Sobotka, A.A. and I. Tempera *PARP1 as an Epigenetic Modulator: Implications for the Regulation of Host-Viral Dynamics*. Pathogens, 2024. **13**, DOI: 10.3390/pathogens13020131.
13. Swindall, A.F., J.A. Stanley, and E.S. Yang *PARP-1: Friend or Foe of DNA Damage and Repair in Tumorigenesis?* Cancers, 2013. **5**, 943-958 DOI: 10.3390/cancers5030943.
14. Chang, H.H.Y., et al., *Non-homologous DNA end joining and alternative*

doi:10.6342/NTU202502570

pathways to double-strand break repair. Nature Reviews Molecular Cell Biology, 2017. **18**(8): p. 495-506.
15. Wang, Y.-L., et al., *Liquid-liquid phase separation in DNA double-strand breaks repair.* Cell Death & Disease, 2023. **14**(11): p. 746.
16. Miné-Hattab, J., S. Liu, and A. Taddei *Repair Foci as Liquid Phase Separation: Evidence and Limitations*. Genes, 2022. **13**, DOI: 10.3390/genes13101846.
17. Bader, A.S., et al., *The roles of RNA in DNA double-strand break repair.* British Journal of Cancer, 2020. **122**(5): p. 613-623.
18. Michelini, F., et al., *Damage-induced lncRNAs control the DNA damage response through interaction with DDRNAs at individual double-strand breaks.* Nature Cell Biology, 2017. **19**(12): p. 1400-1411.
19. Pessina, F., et al., *Functional transcription promoters at DNA double-strand breaks mediate RNA-driven phase separation of damage-response factors.* Nature Cell Biology, 2019. **21**(10): p. 1286-1299.
20. Xiang, Y., et al., *RNA m6A methylation regulates the ultraviolet-induced DNA damage response.* Nature, 2017. **543**(7646): p. 573-576.
21. Xhemalçe, B., K.M. Miller, and N. Gromak, *Epitranscriptome in action: RNA modifications in the DNA damage response.* Mol Cell, 2024. **84**(19): p. 3610-3626.
22. Grossman, E., O. Medalia, and M. Zwerger, *Functional architecture of the nuclear pore complex.* Annu Rev Biophys, 2012. **41**: p. 557-84.
23. Mao, Y.S., B. Zhang, and D.L. Spector, *Biogenesis and function of nuclear bodies.* Trends in Genetics, 2011. **27**(8): p. 295-306.
24. Buchan, J.R. and R. Parker, *Eukaryotic Stress Granules: The Ins and Outs of Translation.* Molecular Cell, 2009. **36**(6): p. 932-941.
25. Alberti, S., A. Gladfelter, and T. Mittag, *Considerations and Challenges in Studying Liquid-Liquid Phase Separation and Biomolecular Condensates.* Cell, 2019. **176**(3): p. 419-434.
26. Sabari, B.R., *Biomolecular Condensates and Gene Activation in Development and Disease.* Developmental Cell, 2020. **55**(1): p. 84-96.
27. Li, J., et al., *Post-translational modifications in liquid-liquid phase separation: a comprehensive review.* Molecular Biomedicine, 2022. **3**(1): p. 13.
28. Pullara, P., I. Alshareedah, and P.R. Banerjee, *Temperature-dependent reentrant phase transition of RNA-polycation mixtures.* Soft Matter, 2022. **18**(7): p. 1342-1349.
29. Wang, B., et al., *Liquid–liquid phase separation in human health and diseases.*

doi:10.6342/NTU202502570

Signal Transduction and Targeted Therapy, 2021. **6**(1): p. 290.
30. Liu, Y., et al., *Crosstalk between protein post-translational modifications and phase separation.* Cell Communication and Signaling, 2024. **22**(1): p. 110.
31. Singatulina, A.S., et al., *PARP-1 Activation Directs FUS to DNA Damage Sites to Form PARG-Reversible Compartments Enriched in Damaged DNA.* Cell Reports, 2019. **27**(6): p. 1809-1821.e5.
32. Wegmann, S., et al., *Tau protein liquid–liquid phase separation can initiate tau aggregation.* The EMBO Journal, 2018. **37**(7): p. e98049.
33. Onuchic, P.L., et al., *Divalent cations can control a switch-like behavior in heterotypic and homotypic RNA coacervates.* Scientific Reports, 2019. **9**(1): p. 12161.
34. Rayman, J.B., K.A. Karl, and E.R. Kandel, *TIA-1 Self-Multimerization, Phase Separation, and Recruitment into Stress Granules Are Dynamically Regulated by Zn2+.* Cell Reports, 2018. **22**(1): p. 59-71.
35. Kilic, S., et al., *Phase separation of 53BP1 determines liquid‐like behavior of DNA repair compartments.* The EMBO Journal, 2019. **38**(16): p. e101379.
36. Boija, A., et al., *Transcription Factors Activate Genes through the Phase-Separation Capacity of Their Activation Domains.* Cell, 2018. **175**(7): p. 1842-1855.e16.
37. Sabari, B.R., et al., *Coactivator condensation at super-enhancers links phase separation and gene control.* Science, 2018. **361**(6400).
38. Lu, H., et al., *Phase-separation mechanism for C-terminal hyperphosphorylation of RNA polymerase II.* Nature, 2018. **558**(7709): p. 318-323.
39. Gibson, B.A., et al., *Organization of Chromatin by Intrinsic and Regulated Phase Separation.* Cell, 2019. **179**(2): p. 470-484.e21.
40. Du, M. and Z.J. Chen, *DNA-induced liquid phase condensation of cGAS activates innate immune signaling.* Science, 2018. **361**(6403): p. 704-709.
41. Chen, X., et al., *Phase separation at the synapse.* Nature Neuroscience, 2020. **23**(3): p. 301-310.
42. Fijen, C. and E. Rothenberg, *The evolving complexity of DNA damage foci: RNA, condensates and chromatin in DNA double-strand break repair.* DNA Repair (Amst), 2021. **105**: p. 103170.
43. Wang, Y.L., et al., *Liquid-liquid phase separation in DNA double-strand breaks repair.* Cell Death Dis, 2023. **14**(11): p. 746.

doi:10.6342/NTU202502570

44. Levone, B.R., et al., *FUS-dependent liquid-liquid phase separation is important for DNA repair initiation.* J Cell Biol, 2021. **220**(5).
45. Wei, M., et al., *SENP1 Decreases RNF168 Phase Separation to Promote DNA Damage Repair and Drug Resistance in Colon Cancer.* Cancer Res, 2023. **83**(17): p. 2908-2923.
46. Ghodke, I., et al., *AHNAK controls 53BP1-mediated p53 response by restraining 53BP1 oligomerization and phase separation.* Molecular Cell, 2021. **81**(12): p. 2596-2610.e7.
47. Zhang, L., et al., *53BP1 regulates heterochromatin through liquid phase separation.* Nature Communications, 2022. **13**(1): p. 360.
48. Fan, X.J., et al., *NONO phase separation enhances DNA damage repair by accelerating nuclear EGFR-induced DNA-PK activation.* Am J Cancer Res, 2021. **11**(6): p. 2838-2852.
49. Altmeyer, M., et al., *Liquid demixing of intrinsically disordered proteins is seeded by poly(ADP-ribose).* Nature Communications, 2015. **6**(1): p. 8088.
50. Pessina, F., et al., *DNA Damage Triggers a New Phase in Neurodegeneration.* Trends in Genetics, 2021. **37**(4): p. 337-354.
51. Boeynaems, S., et al., *Protein Phase Separation: A New Phase in Cell Biology.* Trends in Cell Biology, 2018. **28**(6): p. 420-435.
52. Teixeira, D., et al., *Processing bodies require RNA for assembly and contain nontranslating mRNAs.* Rna, 2005. **11**(4): p. 371-82.
53. Machyna, M., P. Heyn, and K.M. Neugebauer, *Cajal bodies: where form meets function.* Wiley Interdiscip Rev RNA, 2013. **4**(1): p. 17-34.
54. Galganski, L., M.O. Urbanek, and W.J. Krzyzosiak, *Nuclear speckles: molecular organization, biological function and role in disease.* Nucleic Acids Research, 2017. **45**(18): p. 10350-10368.
55. Cheutin, T., et al., *Maintenance of stable heterochromatin domains by dynamic HP1 binding.* Science, 2003. **299**(5607): p. 721-5.
56. Chu, L., et al., *The Spatiotemporal Dynamics of Chromatin Protein HP1α Is Essential for Accurate Chromosome Segregation during Cell Division*.* Journal of Biological Chemistry, 2014. **289**(38): p. 26249-26262.
57. Keenen, M.M., et al., *HP1 proteins compact DNA into mechanically and positionally stable phase separated domains.* eLife, 2021. **10**: p. e64563.
58. Larson, A.G., et al., *Liquid droplet formation by HP1α suggests a role for phase separation in heterochromatin.* Nature, 2017. **547**(7662): p. 236-240.

doi:10.6342/NTU202502570

59. Strom, A.R., et al., *Phase separation drives heterochromatin domain formation.* Nature, 2017. **547**(7662): p. 241-245.
60. Maharana, S., et al., *RNA buffers the phase separation behavior of prion-like RNA binding proteins.* Science, 2018. **360**(6391): p. 918-921.
61. Chen, Q., et al., *Phosphorylation and specific DNA improved the incorporation ability of p53 into functional condensates.* International Journal of Biological Macromolecules, 2023. **230**: p. 123221.
62. Kovachev, P.S., et al., *Distinct modulatory role of RNA in the aggregation of the tumor suppressor protein p53 core domain.* Journal of Biological Chemistry, 2017. **292**(22): p. 9345-9357.
63. Shrinivas, K., et al., *Enhancer Features that Drive Formation of Transcriptional Condensates.* Molecular Cell, 2019. **75**(3): p. 549-561.e7.
64. Shelkovnikova, T.A., et al., *Recruitment into stress granules prevents irreversible aggregation of FUS protein mislocalized to the cytoplasm.* Cell Cycle, 2013. **12**(19): p. 3383-3391.
65. Shakya, A. and J.T. King, *DNA Local-Flexibility-Dependent Assembly of Phase-Separated Liquid Droplets.* Biophysical Journal, 2018. **115**(10): p. 1840-1847.
66. Gao, J., et al., *G-quadruplex DNA inhibits unwinding activity but promotes liquid-liquid phase separation by the DEAD-box helicase Ded1p.* Chem Commun (Camb), 2021. **57**(60): p. 7445-7448.
67. Ishiguro, A., et al., *ALS-linked FUS mutations dysregulate G-quadruplex-dependent liquid–liquid phase separation and liquid-to-solid transition.* Journal of Biological Chemistry, 2021. **297**(5): p. 101284.
68. Kim, T.H., et al., *Phospho-dependent phase separation of FMRP and CAPRIN1 recapitulates regulation of translation and deadenylation.* Science, 2019. **365**(6455): p. 825-829.
69. Alshareedah, I., et al., *Phase transition of RNA−protein complexes into ordered hollow condensates.* Proceedings of the National Academy of Sciences, 2020. **117**(27): p. 15650-15658.
70. Asamitsu, S., et al., *CGG repeat RNA G-quadruplexes interact with FMRpolyG to cause neuronal dysfunction in fragile X-related tremor/ataxia syndrome.* Sci Adv, 2021. **7**(3).
71. Chuang, T.-W., K.-M. Lee, and W.-Y. Tarn *Function and Pathological Implications of Exon Junction Complex Factor Y14*. Biomolecules, 2015. **5**, 343-355 DOI: 10.3390/biom5020343.

doi:10.6342/NTU202502570

72. Fukumura, K., et al. *The Exon Junction Complex Controls the Efficient and Faithful Splicing of a Subset of Transcripts Involved in Mitotic Cell-Cycle Progression*. International Journal of Molecular Sciences, 2016. **17**, DOI: 10.3390/ijms17081153.
73. Wang, Z., V. Murigneux, and H. Le Hir, *Transcriptome-wide modulation of splicing by the exon junction complex.* Genome Biology, 2014. **15**(12): p. 551.
74. Hsu Ia, W., et al., *Phosphorylation of Y14 modulates its interaction with proteins involved in mRNA metabolism and influences its methylation.* J Biol Chem, 2005. **280**(41): p. 34507-12.
75. Lu, C.-C., et al., *Y14 governs p53 expression and modulates DNA damage sensitivity.* Scientific Reports, 2017. **7**(1): p. 45558.
76. Mao, H., et al., *Rbm8a haploinsufficiency disrupts embryonic cortical development resulting in microcephaly.* J Neurosci, 2015. **35**(18): p. 7003-18.
77. Mao, H., et al., *Haploinsufficiency for Core Exon Junction Complex Components Disrupts Embryonic Neurogenesis and Causes p53-Mediated Microcephaly.* PLoS Genet, 2016. **12**(9): p. e1006282.
78. Su, C.-H., et al., *The Y14-p53 regulatory circuit in megakaryocyte differentiation and thrombocytopenia.* iScience, 2021. **24**(11): p. 103368.
79. Chuang, T.-W., et al., *The RNA Processing Factor Y14 Participates in DNA Damage Response and Repair.* iScience, 2019. **13**: p. 402-415.
80. Chuang, T.-W., et al., *LncRNA HOTAIRM1 functions in DNA double-strand break repair via its association with DNA repair and mRNA surveillance factors.* Nucleic Acids Research, 2023. **51**(7): p. 3166-3184.
81. Yu, C.L., et al., *Co-phase separation of Y14 and RNA in vitro and its implication for DNA repair.* Rna, 2023. **29**(7): p. 1007-1019.
82. Hsu, I.-W., et al., *Phosphorylation of Y14 Modulates Its Interaction with Proteins Involved in mRNA Metabolism and Influences Its Methylation*.* Journal of Biological Chemistry, 2005. **280**(41): p. 34507-34512.
83. Gai, X., et al., *Pre-ribosomal RNA reorganizes DNA damage repair factors in nucleus during meiotic prophase and DNA damage response.* Cell Research, 2022. **32**(3): p. 254-268.
84. Wang, Y.-L., et al., *MRNIP condensates promote DNA double-strand break sensing and end resection.* Nature Communications, 2022. **13**(1): p. 2638.
85. Ulianov, S.V., et al., *Suppression of liquid–liquid phase separation by 1,6-hexanediol partially compromises the 3D genome organization in living cells.*

doi:10.6342/NTU202502570

Nucleic Acids Research, 2021. **49**(18): p. 10524-10541.
86. Tacke, R. and J.L. Manley, *Determinants of SR protein specificity.* Current Opinion in Cell Biology, 1999. **11**(3): p. 358-362.
87. Zahler, A.M., et al., *SR proteins: a conserved family of pre-mRNA splicing factors.* Genes Dev, 1992. **6**(5): p. 837-47.
88. André, A.A.M. and E. Spruijt, *Liquid–Liquid Phase Separation in Crowded Environments.*
89. Banani, S.F., et al., *Biomolecular condensates: organizers of cellular biochemistry.* Nature Reviews Molecular Cell Biology, 2017. **18**(5): p. 285-298.
90. Mao, A.H., et al., *Net charge per residue modulates conformational ensembles of intrinsically disordered proteins.* Proc Natl Acad Sci U S A, 2010. **107**(18): p. 8183-8.
91. Qu, F., P.S. Tsegay, and Y. Liu, *N(6)-Methyladenosine, DNA Repair, and Genome Stability.* Front Mol Biosci, 2021. **8**: p. 645823.
92. Dominissini, D., et al., *Topology of the human and mouse m6A RNA methylomes revealed by m6A-seq.* Nature, 2012. **485**(7397): p. 201-206.
93. Jiang, A., et al., *RBM15 condensates modulate m6A modification of STYK1 to promote tumorigenesis.* Computational and Structural Biotechnology Journal, 2022. **20**: p. 4825-4836.
94. Su, Y., et al., *Modulation of Phase Separation by RNA: A Glimpse on N(6)-Methyladenosine Modification.* Front Cell Dev Biol, 2021. **9**: p. 786454.
95. Liao, S., H. Sun, and C. Xu, *YTH Domain: A Family of N6-Methyladenosine (m6A) Readers.* Genomics, Proteomics & Bioinformatics, 2018. **16**(2): p. 99-107.
96. Krietsch, J., et al., *PARP activation regulates the RNA-binding protein NONO in the DNA damage response to DNA double-strand breaks.* Nucleic Acids Research, 2012. **40**(20): p. 10287-10301.
97. Mamontova, E.M., et al., *FUS RRM regulates poly(ADP-ribose) levels after transcriptional arrest and PARP-1 activation on DNA damage.* Cell Reports, 2023. **42**(10): p. 113199.
98. Ray Chaudhuri, A. and A. Nussenzweig, *The multifaceted roles of PARP1 in DNA repair and chromatin remodelling.* Nature Reviews Molecular Cell Biology, 2017. **18**(10): p. 610-621.
99. Chappidi, N., et al., *PARP1-DNA co-condensation drives DNA repair site assembly to prevent disjunction of broken DNA ends.* Cell, 2024. **187**(4): p. 945-961.e18.

doi:10.6342/NTU202502570

100. Dawicki-McKenna, Jennine M., et al., *PARP-1 Activation Requires Local Unfolding of an Autoinhibitory Domain.* Molecular Cell, 2015. **60**(5): p. 755-768.
101. Lu, R., et al. *Post-Translational Modification of MRE11: Its Implication in DDR and Diseases*. Genes, 2021. **12**, DOI: 10.3390/genes12081158.
102. Chowdhury, S.G., et al., *NHEJ is promoted by the phosphorylation and phosphatase activity of PTEN via regulation of DNA-PKcs.* Biochimica et Biophysica Acta (BBA) - Molecular Cell Research, 2024. **1871**(8): p. 119828.
103. Ali, A.A.E., et al., *Specific recognition of a multiply phosphorylated motif in the DNA repair scaffold XRCC1 by the FHA domain of human PNK.* Nucleic Acids Research, 2009. **37**(5): p. 1701-1712.
104. Maeshima, K., et al., *A Transient Rise in Free Mg2+ Ions Released from ATP-Mg Hydrolysis Contributes to Mitotic Chromosome Condensation.* Current Biology, 2018. **28**(3): p. 444-451.e6.
105. Sukhanova, M.V., et al., *Divalent and multivalent cations control liquid-like assembly of poly(ADP-ribosyl)ated PARP1 into multimolecular associates in vitro.* Communications Biology, 2024. **7**(1): p. 1148.
106. Singh, V., et al., *Zinc promotes liquid–liquid phase separation of tau protein.* Journal of Biological Chemistry, 2020. **295**(18): p. 5850-5856.
107. Dutagaci, B., et al., *Charge-driven condensation of RNA and proteins suggests broad role of phase separation in cytoplasmic environments.* Elife, 2021. **10**.
108. Yao, R.-W., et al., *Nascent Pre-rRNA Sorting via Phase Separation Drives the Assembly of Dense Fibrillar Components in the Human Nucleolus.* Molecular Cell, 2019. **76**(5): p. 767-783.e11.
109. Jiang, L., et al., *NEAT1 scaffolds RNA-binding proteins and the Microprocessor to globally enhance pri-miRNA processing.* Nature Structural & Molecular Biology, 2017. **24**(10): p. 816-824.
110. Zeng, M., et al., *Phase Transition in Postsynaptic Densities Underlies Formation of Synaptic Complexes and Synaptic Plasticity.* Cell, 2016. **166**(5): p. 1163-1175.e12.
111. Liu, Z., et al., *Par complex cluster formation mediated by phase separation.* Nature Communications, 2020. **11**(1): p. 2266.
112. Wang, H., et al., *Temporal and spatial assembly of inner ear hair cell ankle link condensate through phase separation.* Nature Communications, 2023. **14**(1): p. 1657.
113. Zeng, M., et al., *Reconstituted Postsynaptic Density as a Molecular Platform for*

doi:10.6342/NTU202502570

Understanding Synapse Formation and Plasticity. Cell, 2018. **174**(5): p. 1172-1187.e16.

114. Gruijs da Silva, L.A. and D. Dormann, *Sedimentation Assays to Assess the Impact of Posttranslational Modifications on Phase Separation of RNA-Binding Proteins In Vitro and In Cells*, in *Phase-Separated Biomolecular Condensates: Methods and Protocols*, H.-X. Zhou, J.-H. Spille, and P.R. Banerjee, Editors. 2023, Springer US: New York, NY. p. 325-339.

115. Gruijs da Silva, L.A., et al., *Disease-linked TDP-43 hyperphosphorylation suppresses TDP-43 condensation and aggregation.* The EMBO Journal, 2022. **41**(8): p. e108443.

doi:10.6342/NTU202502570